POLITECNICO DI TORINO

Master's Degree
in Mathematical Engineering

Master's Degree Thesis

Theoretical biophysics of liquid-liquid phase separation in the nucleolus

Supervisors
Prof. Lamberto Rondoni
Dr. Anna Erzberger
Dr. Roman Belousov
Dr. Yuki Hayashi

Candidate
Michele Lupini

Academic Year 2024-2025

Ai miei genitori
† Ai miei nonni

Summary

Phase separation is a fundamental physical mechanism that drives the organization of many complex systems. Specifically, in biology cells are thought to exploit this mechanism to organize their internal structure and to compartmentalize biochemical processes within membraneless organelles. Nucleoli—one of such organelles in eukaryotes—are known to form hierarchical subcompartments dedicated to ribosomal RNA (rRNA) transcription, processing, and ribosome assembly. The underlying mechanism of these processes and their biological significance remain unknown. Perturbations of rRNA transcription, e.g. in laboratory experiments, reorganises the nucleolar structure. Perturbations of rRNA transcription, e.g. in laboratory experiments, reorganises the nucleolar structure. Quantitative live-cell imaging after inhibition of rRNA transcription reveals two steps of reorganization consisting in, first, fusion of individual subunits, then followed by, second stage, their exposure to the nucleolar surface. To model the formation of nucleolar subcompartments, we develop a theoretical framework based on Flory-Huggins theory of phase separation in multicomponent solutions and Cahn-Hilliard dynamics. To fit this family of models to experimental observations, we design several estimation techniques, which help identify the plausible values of key physical parameters from high-resolution imaging data. By applying this technique we test whether the phenomenology of phase separation in liquid solutions is sufficient to explain formation of the nucleolar structure.

Acknowledgements

This work wouldn't have been possible without the support, guidance and kindness of many people along the way.

First, I want to sincerely thank Prof. Lamberto Rondoni, who not only guided me through my academic path at Politecnico di Torino, but also encouraged me to pursue my thesis at EMBL. His advice, support and enthusiasm for research have been invaluable throughout this journey.

A heartfelt thank you to Dr. Anna Erzberger and Dr. Roman Belousov, who supervised my work at EMBL and provided insightful guidance at every stage of this project. Their expertise, patience and encouragement have greatly enriched my experience. I am also grateful to the entire Erzberger Group, for their collaboration and for making the lab such a stimulating research environment. A special thanks to Dr. Yuki Hayashi, who generously provided experimental data and shared his expertise on the biological aspects of the project. His help has been essential in connecting the theoretical and experimental sides of this work. I would also like to thank the Cuylen Group for their kindness and for making me feel welcome during my time at EMBL. Beyond the research, I grateful to everyone at EMBL who made this experience so rewarding, both scientifically and personally. The supportive and friendly atmosphere made my time there truly special.

I am deeply thankful to my friends, whose presence, conversations and encouragement have been a constant source of motivation throughout this journey. Distance was never a barrier for many and I truly appreciate their effort in staying present, always making me feel welcomed whenever I was back. A special mention goes to my flatmates, who have shared this time with me in many different ways. Their company, humor, and occasional chaos have all been part of the experience and for that, I am grateful.

Finally, I want to express my heartfelt gratitude to my family, whose constant encouragement and unwavering belief in me have made all of this possible. Thank you for shaping me into the person I am.

Contents

List of Tables

List of Figures

Chapter 1

Introduction

A homogeneous mixture of components, that spontaneously demixes into distinct phases with different compositions, undergoes a physical process called phase separation. This phenomenon encompasses a natural formation of distinct compartments with different macroscopic characteristics. Phase separation occurs in liquid solution when molecular interactions favor the segregation of specific components, overcoming the entropic tendency of the system to remain mixed [4, 8, 14, 15, 31]. One example that we can experience in our everyday life is the separation of water and oil. When these two liquids are combined, they initially form a heterogeneous mixture. Over time hydrophobic oil molecules and water repel each other forming two separate phases.

Phase separation typically starts with nucleation, which is the process where small unstable clusters of molecules aggregate forming small droplets. These droplets are then increasing in size through their fusion or growth at the expense of smaller droplets—the phenomenon called Ostwald ripening [23]. The droplets' coarsening process continues until the system reaches a steady state.

The dynamics of spontaneous phase separation phenomena have been studied in various research fields and developed applications especially in material science [20, 26]. Applications of broad interest include design of polymer mixtures for electronic devices, such as organic solar cells [7] and organic memory diodes [1], and assembly of synthetic membranes for electro-optical devices [18, 19].

The principles of phase separation, developed for material science, directly apply to biological systems [22]. These principles shed light on the important questions in biology: how do the cells organize distinct intracellular compartments to facilitate complex biochemical reactions? Many biological processes require isolated chemical microenvironments that are physically separated from their surroundings, but capable to exchange signaling molecules and reaction products with the environment.

One example ubiquitously found in cells is the formation of membrane-bound organelles, physically isolating compartments by lipid membrane. In addition, cells contain diverse membraneless organelles that form without physical barriers. Recent studies suggest that most membraneless organelles exhibit liquid-like properties and can be treated as droplets of a liquid-liquid phase separation phenomenon [12, 27, 29, 30, 32]. A notable example of membraneless organelles is the nucleolus—the largest structure in the nucleus of eukaryotic cell—playing a crucial role in ribosome biogenesis and known to behave as a liquid [2].

Nucleoli exhibit a nested multiphase organisation, which is crucial for separating distinct steps of ribosome biogenesis. Structurally, the nucleolus is subdivided into three subcompartments: the fibrillar center (FC), the dense fibrillar component (DFC), and the granular component (GC). The FC comprises of RNA polymerase I and its transcription factors, serving as the primary site of rRNA transcription. The DFC surrounds the FC and is responsible for maturation of rRNA by processing and modification of newly transcribed rRNA. The outermost GC is the site of the final stages of pre-ribosomal subunit assembly, where pre-ribosomal particles undergo maturation before being exported to the cytoplasm for protein synthesis. Thus, subcompartmentalization of the nucleolus is tightly coupled to the production of ribosomes, and loss of its structural integrity can impair protein synthesis, leading to cellular dysfunction.

Pursuing the hypothesis that the liquid-liquid phase separation drives formation of the nucleoli structure, in this work we seek to build a quantitative model for our imaging data [11], which would provide further physical insights into understanding of nucleolar organization. To achieve this, we develop a theoretical framework grounded on Flory-Huggins theory of phase separation in multicomponent solutions and Cahn-Hilliard dynamics to describe to describe the system's evolution in time.

By integrating theoretical modeling with data-driven parameter estimation, this work aims to bridge the gap between experimental observations and the underlying physical mechanisms governing nucleolar organization. To this end we explore various inference techniques for the key modeling parameters under the assumption, that the imaging data present an equilibrium state. We validate our approach by applying the estimation procedure to equilibrium states generated from known parameter values. Finally, we apply our framework to experimental imaging data from [11], assessing its ability to accurately capture nucleolar phase behavior.

Our analysis reveals that the equilibrium model of a four-component protein solution is not sufficient to explain the formation of the nucleolar structures. This result suggests that additional mechanisms are necessary to stabilize them. Such mechanism may include: (i) rRNA transcription, in which ribosomal RNA (rRNA) is transcribed from ribosomal DNA (rDNA) by RNA polymerase I at the boundary between FC and DFC region [13]; (ii) rRNA processing, which correspond to the maturation of transcribed rRNA, called pre-rRNA, this process cleaves and add post-transcriptional modification of rRNA, generating flow of RNA molecules from nucleolar interior (FC) to exterior (GC and far beyond to the nucleoplasm); (iii) ribosome assembly, where pre-RNA and ribosomial proteins interact to make pre-ribosome particles, that subsequently translocate to the cytoplasm for protein synthesis. Importantly, these nucleolar activities consume cellular energy such as ATP. As rRNA transcription is the most active transcription and subsequent processing and ribosome assembly are a vital for cellular homeostasis, it is believed that nucleolar activity is most energy consuming process. Although we do not explore these extensions of the underlying model and strictly focus on the equilibrium mechanisms, our theoretical and computational toolbox can serve as foundations for further research.

Chapter 2

Modeling liquid-liquid phase separation

A common approach to modeling the dynamics of phase separating liquids is the so called Cahn-Hilliard equations [3, 20, 26, 31]. Given a suitable definition of the system's free energy, these equations are formulated by using a linear constitutive relation and the gradients of the components' chemical potentials.

This Chapter provides an overview of the theoretical framework for liquid-liquid phase separation in mixtures of C components in d-dimensional physical space. The approach that we follow relies on the Flory-Huggins theory of protein solutions [6, 8, 14], which accounts for both local and nonlocal contributions of the system's free energy. A particular attention is dedicated to the spectral formulation of the theory, which provides foundation for the inference method developed and applied in the later chapters.

To model equilibrium states, we describe two complementary approaches. First, we evolve the system by numerically integrating its dynamic equations based on the Cahn-Hilliard framework. Second, we employ Metropolis-Hastings sampling, a Markov chain Monte Carlo method, to generate equilibrium configurations by directly sampling from the Boltzmann distribution of the system. These methods provide two distinct yet interconnected perspectives on equilibrium phase separation systems, one based on deterministic evolution and the other on stochastic sampling. This Chapter lays the groundwork for understanding the mathematical modeling of liquid-liquid phase separation and provides the necessary tools for generating equilibrium states, which will be central for testing the inference techniques explored in subsequent chapters.

2.1 Flory-Huggins theory of phase separation in multicomponent solutions

In general we consider an incompressible mixture of C components distributed over a rectangular spatial domain $\Omega \subset \mathbb{R}^d$, with $d = 1,2,3$. The particles of each component, labeled by $\mathcal{A} = \{1, \dots, C\}$, collectively occupy the volume of the entire domain—without leaving empty spaces. An extension of the theory, in which empty space is modeled as an additional component is also possible.

Following the Flory-Huggins theory [8, 14], we assume that each molecule occupies a constant volume v_a. Here we adopt the convention that the solvent is labeled by $a = C$. Sizes of the other molecules can then be expressed by a dimensionless number $N_a = v_a / v_C$.

With the above assumption we can describe the system's state by volume fractions $\phi_a(\boldsymbol{x})$, which a^{th} component occupies in the neighborhood of a point $\boldsymbol{x} \in \Omega$. The distribution of molecules in the form of concentrations can thus be obtained from $c_a(\boldsymbol{x}) = \phi_a(\boldsymbol{x})/(N_a v_C)$. In addition the volume fractions of all components must satisfy

$$\sum_{a \in \mathcal{A}} \phi_a(\boldsymbol{x}) = 1, \tag{2.1}$$

which reduces by one the number of fields required to specify a unique state of the system.

Hence at each instant of time t the system's configuration is uniquely identified by the vector of $C-1$ scalar fields $\phi_{a=1,2,\ldots,C-1}(\boldsymbol{x}, t)$, whereas the distribution of solvent is determined from Eq. (2.1):

$$\phi_C(\boldsymbol{x}, t) = 1 - \sum_{a \in \mathcal{A}_C} \phi_a(\boldsymbol{x}, t), \tag{2.2}$$

where $\mathcal{A}_C = \mathcal{A} \setminus \{C\}$ denotes the set of all labels except C.

The Flory-Huggins free energy F of a multicomponent mixture can then be cast in reduced energy units of $k_{\mathrm{B}}T$, with Boltzmann constant k_{B} and temperature T, as a functional of the volume fractions' vector $\boldsymbol{\phi} = \{\phi_a\}_{a \in \mathcal{A}_C}$:

$$F[\boldsymbol{\phi}] = \int_\Omega f\Big(\boldsymbol{\phi}(\boldsymbol{x}), \nabla\boldsymbol{\phi}(\boldsymbol{x})\Big)\, \boldsymbol{dx}, \tag{2.3}$$

where the spatial integration spans the whole domain Ω, and $\nabla\boldsymbol{\phi}$ denotes the component-wise gradient of $\boldsymbol{\phi}$, so that $(\nabla\boldsymbol{\phi})_a = \nabla\phi_a$. The energy-density is further split into local and nonlocal contributions, respectively:

$$f(\boldsymbol{\phi}, \nabla\boldsymbol{\phi}) = f_{\mathrm{loc}}(\boldsymbol{\phi}) + f_{\mathrm{nonloc}}(\nabla\boldsymbol{\phi}).$$

The local term of the Flory-Huggins free energy takes the form

$$\begin{aligned} f_{\mathrm{loc}}(\boldsymbol{\phi}) = \sum_{a \in \mathcal{A}_C} \frac{\phi_a}{N_a} \log \phi_a + \frac{1 - \sum_{a \in \mathcal{A}_C} \phi_a}{N_C} \log\left(1 - \sum_{a \in \mathcal{A}_C} \phi_a\right) \\ + \frac{1}{2} \sum_{a,b \in \mathcal{A}_C} \chi_{ab}\phi_a\phi_b + \sum_{a \in \mathcal{A}_C} \chi_{aC}\phi_a \left(1 - \sum_{a \in \mathcal{A}_C} \phi_a\right), \end{aligned} \tag{2.4}$$

in which $N_C = 1$ and Eq. (2.2) are used, whereas the coefficients χ_{ab} form a symmetric matrix $\chi_{ab} = \chi_{ba}$ such that $\chi_{aa} = 0$. The nonlocal contribution of the energy density $f(\boldsymbol{\phi})$ is given by

$$f_{\mathrm{nonloc}}(\nabla\boldsymbol{\phi}) = \frac{1}{2} \sum_{a,b \in \mathcal{A}} \lambda_{ab} \nabla\phi_a \cdot \nabla\phi_b.$$

in which the symmetric coefficients $\lambda_{ab} = \lambda_{ba}$ penalizes spatial inhomogeneities [31]. With help of Eq. (2.2) the nonlocal term can be further simplified as follows

$$\begin{aligned} f_{\text{nonloc}}(\nabla\boldsymbol{\phi}) &= \frac{1}{2}\sum_{a,b\in\mathcal{A}_C}\lambda_{ab}\nabla\phi_a\cdot\nabla\phi_b + \sum_{a\in\mathcal{A}_C}\lambda_{aC}\nabla\phi_a\cdot\nabla\left(1-\sum_{b\in\mathcal{A}_C}\phi_b\right) \\ &\quad + \frac{1}{2}\lambda_{CC}\left|\nabla\left(1-\sum_{b\in\mathcal{A}_C}\phi_b\right)\right|^2 \\ &= \frac{1}{2}\sum_{a,b\in\mathcal{A}_C}\lambda_{ab}\nabla\phi_a\cdot\nabla\phi_b - \sum_{a,b\in\mathcal{A}_C}\lambda_{aC}\nabla\phi_a\cdot\nabla\phi_b \\ &\quad + \frac{1}{2}\lambda_{CC}\sum_{a,b\in\mathcal{A}_C}\nabla\phi_a\cdot\nabla\phi_b \\ &= \frac{1}{2}\sum_{a,b\in\mathcal{A}_C}\kappa_{ab}\nabla\phi_a\cdot\nabla\phi_b, \end{aligned} \tag{2.5}$$

in which we introduced

$$\kappa_{ab} := \lambda_{ab} + \lambda_{CC} - \lambda_{aC} - \lambda_{bC}.$$

Note that the coefficients κ_{ab} form a symmetric matrix $\kappa_{ab} = \kappa_{ba}$, with $(C-1)(C-1)$ elements for $a, b \in \mathcal{A}_C$.

Hence the free energy depends on $C-1$ constants $N_{a\neq C}$, and $C(C-1)/2$ coefficients $\chi_{a<b}$ $(a, b \in \mathcal{A})$ and $C(C-1)/2$ coefficients $\kappa_{a\leq b}$ $(a, b \in \mathcal{A}_C)$. Moreover, substituting the local contribution (2.4) and the nonlocal contribution (2.5) into Eq. (2.3), the free energy can be explicitly written as

$$\begin{aligned} F[\boldsymbol{\phi}] = \int_\Omega \boldsymbol{dx}\, \Bigg[&\sum_{a\in\mathcal{A}_C}\frac{\phi_a}{N_a}\log\phi_a + \frac{1-\sum_{a\in\mathcal{A}_C}\phi_a}{N_C}\log\left(1-\sum_{a\in\mathcal{A}_C}\phi_a\right) \\ &+ \frac{1}{2}\sum_{a,b\in\mathcal{A}_C}\left(\chi_{ab}\phi_a\phi_b + \kappa_{ab}\nabla\phi_a\cdot\nabla\phi_b\right) + \sum_{a\in\mathcal{A}_C}\chi_{aC}\phi_a\left(1-\sum_{a\in\mathcal{A}_C}\phi_a\right)\Bigg]. \end{aligned} \tag{2.6}$$

2.2 Cahn-Hilliard dynamics

Phase-separating systems, such as those modeled by Cahn-Hilliard dynamics [3, 26, 31], describe the evolution of volume fraction fields in multicomponent mixtures. These systems evolve towards equilibrium through diffusive transport, driven by chemical potential gradients.

The evolution of the volume fractions $\boldsymbol{\phi} = \{\phi_a\}_{a\in\mathcal{A}_C}$ is governed by the continuity equations for $a \in \mathcal{A}_C$

$$\partial_t\phi_a = -\nabla\cdot\boldsymbol{j}_a \tag{2.7}$$

where $\boldsymbol{j}_a = \boldsymbol{j}_a(\boldsymbol{\phi})$ represent the flux of component a.

We assume a linear constitutive relation where the flux $\boldsymbol{j}_a$ is proportional to the gradient of the chemical potential $\mu_a = \mu_a(\boldsymbol{\phi})$:

$$\boldsymbol{j}_a = -\Lambda_a \nabla \mu_a, \tag{2.8}$$

where $\Lambda_a = \Lambda_a(\boldsymbol{\phi}) > 0$ is the diffusion coefficient, which, in general, is a function of the volume fractions $\boldsymbol{\phi}$ and may be different for each component $a \in \mathcal{A}_C$.

As a specific example, if $\Lambda_a = \Lambda$ is constant and identical for each component $a \in \mathcal{A}$, the flux simplifies to $\boldsymbol{j}_a = -\Lambda \nabla \mu_a$, leading to the equation

$$\partial_t \phi_a = \Lambda \nabla^2 \mu_a.$$

Alternatively, if we consider a diffusion coefficient proportional to the corresponding volume fraction, such that $\Lambda_a(\boldsymbol{\phi}) = D\phi_a$ with D constant, the flux becomes $\boldsymbol{j}_a = -D\phi_a \nabla \mu_a$ and the evolution equation takes the form

$$\partial_t \phi_a = D \nabla \cdot \left(\phi_a \nabla \mu_a\right).$$

On the other hand, the chemical potential is the variation of the free energy functional (2.6), which here is borrowed from the Flory-Huggins theory. In this context, we define the chemical potential for the component $a \in \mathcal{A}_C$ as the functional derivative of the free energy F with respect to the volume fraction ϕ_a, such that

$$\begin{aligned} \mu_a = \frac{\delta F}{\delta \phi_a} &:= \partial_{\phi_a} f - \nabla \cdot \partial_{\nabla \phi_a} f \\ &= \partial_{\phi_a} f_{\text{loc}} - \nabla \cdot \partial_{\nabla \phi_a} f_{\text{nonloc}}. \end{aligned}$$

Together the continuity equation (2.7) and the constitutive relation (2.8) yield a system of equations for Cahn-Hilliard dynamics. Assuming that χ_{ab}, κ_{ab} and N_a are constants, independent of space and volume fractions, one can directly compute each term of the expression. For each $a \in \mathcal{A}_C$, the local term gives

$$\begin{aligned} \partial_{\phi_a} f_{\text{loc}}(\boldsymbol{\phi}) = \partial_{\phi_a} \Bigg\{ &\sum_{b \in \mathcal{A}_C} \frac{\phi_b}{N_b} \log \phi_b + \frac{1 - \sum_{b \in \mathcal{A}_C} \phi_b}{N_C} \log \left(1 - \sum_{b \in \mathcal{A}_C} \phi_b\right) \\ &+ \frac{1}{2} \sum_{b,c \in \mathcal{A}_C} \chi_{bc} \phi_b \phi_c + \sum_{b \in \mathcal{A}_C} \chi_{bC} \phi_b \left(1 - \sum_{c \in \mathcal{A}_C} \phi_c\right) \Bigg\} \\ = &\frac{1 + \log \phi_a}{N_a} - \frac{1 + \log\left(1 - \sum_{b \in \mathcal{A}_C} \phi_b\right)}{N_C} \\ &+ \sum_{b \in \mathcal{A}_C} \chi_{ab} \phi_b + \chi_{aC} \left(1 - \sum_{b \in \mathcal{A}_C} \phi_b\right) - \sum_{b \in \mathcal{A}_C} \chi_{bC} \phi_b \\ = &\frac{1 + \log \phi_a}{N_a} - \frac{1 + \log\left(1 - \sum_{b \in \mathcal{A}_C} \phi_b\right)}{N_C} + \sum_{b \in \mathcal{A}_C} \left(\chi_{ab} - \chi_{bC} - \chi_{aC}\right) \phi_b + \chi_{aC}. \end{aligned}$$

Similarly, for the nonlocal term, we get

$$\begin{aligned}\partial_{\nabla\phi_a} f_{\text{nonloc}}(\nabla\boldsymbol{\phi}) &= \partial_{\nabla\phi_a}\left\{\frac{1}{2}\sum_{b,c\in\mathcal{A}_C}\kappa_{bc}\nabla\phi_b\cdot\nabla\phi_c\right\}\\ &= \sum_{b\in\mathcal{A}_C}\kappa_{ab}\nabla\phi_b.\end{aligned}$$

Finally, we write the dynamic equations for $a \in \mathcal{A}_C$ as

$$\begin{aligned}\partial_t\phi_a = \nabla\cdot\Bigg\{\Lambda\nabla\Bigg[&\frac{\log\phi_a}{N_a} - \frac{\log\left(1-\sum_{b\in\mathcal{A}_C}\phi_b\right)}{N_C}\\ &+ \sum_{b\in\mathcal{A}_C}\left(\chi_{ab}-\chi_{bC}-\chi_{aC}\right)\phi_b - \sum_{b\in\mathcal{A}_C}\kappa_{ab}\nabla^2\phi_b\Bigg]\Bigg\}.\end{aligned} \tag{2.9}$$

This set of equations describes the evolution of the first $C-1$ volume fractions of the system in time. However, once the scalar fields $\phi_a(\boldsymbol{x},t)$ at time t for each $a \in \mathcal{A}_C$ are determined, then the configuration of the mixture is completely known, since we can directly compute the volume fraction of the C^{th} component at the same time t, through the constraint (2.2).

To verify that this formulation generalizes the binary and ternary mixture cases and is consistent with equations found in the literature [20, 26, 31], we examine the specific cases $C = 2$ and $C = 3$ and confirm that they reproduce the known results.

Binary mixtures Let us consider $\mathcal{A} = \{1{,}2\}$ with $C = 2$, which implies $\mathcal{A}_C = \{1\}$. In this case, the local free energy density simplifies to

$$\begin{aligned}f_{\text{loc}}(\phi_1) &= \frac{\phi_1}{N_1}\log\phi_1 + \frac{1-\phi_1}{N_2}\log\left(1-\phi_1\right) + \frac{1}{2}\chi_{11}\phi_1\phi_1 + \chi_{12}\phi_1\left(1-\phi_1\right)\\ &= \frac{\phi_1}{N_1}\log\phi_1 + \frac{1-\phi_1}{N_2}\log\left(1-\phi_1\right) + \chi_{12}\phi_1\left(1-\phi_1\right),\end{aligned}$$

where we used the fact that $\chi_{aa} = 0$ and the symmetry of χ_{ab}, so that $\chi_{12} = \chi_{21}$. Moreover, the nonlocal contribution reduces to

$$f_{\text{nonloc}}(\nabla\phi_1) = \nabla\phi_1\cdot\kappa_{11}\nabla\phi_1 = \kappa_{11}|\nabla\phi_1|^2,$$

where κ_{11} reduces to a scalar. Similarly, the dynamic equations also coincide with the expectations, as we obtain

$$\begin{aligned}\partial_t\phi_1 &= \nabla\cdot\left\{\Lambda\nabla\left[\frac{\log\phi_1}{N_1} - \frac{\log\left(1-\phi_1\right)}{N_2} + \left(\chi_{11}-\chi_{12}-\chi_{12}\right)\phi_1 - \kappa_{11}\nabla^2\phi_1\right]\right\}\\ &= \nabla\cdot\left\{\Lambda\nabla\left[\frac{\log\phi_1}{N_1} - \frac{\log\left(1-\phi_1\right)}{N_2} - 2\chi_{12}\phi_1 - \kappa_{11}\nabla^2\phi_1\right]\right\},\end{aligned}$$

that matches equations in literature [31], so this confirms the consistency of our general formulation with the binary mixture case.

Ternary mixtures For a ternary mixture, we set $\mathcal{A} = \{1,2,3\}$ and $C = 3$. Then, for $a \in \mathcal{A}_C = \{1,2\}$, dynamical equations (2.9) reduce to

$$\begin{aligned}\partial_t\phi_1 = \nabla \cdot \Bigg\{\Lambda\nabla\Bigg[&\frac{\log\phi_1}{N_1} - \frac{\log(1-\phi_1-\phi_2)}{N_3}\\ &- 2\chi_{13}\phi_1 + (\chi_{12}-\chi_{13}-\chi_{23})\phi_2 - \kappa_{11}\nabla^2\phi_1 - \kappa_{12}\nabla^2\phi_2\Bigg]\Bigg\},\\ \partial_t\phi_2 = \nabla \cdot \Bigg\{\Lambda\nabla\Bigg[&\frac{\log\phi_2}{N_2} - \frac{\log(1-\phi_1-\phi_2)}{N_3}\\ &- 2\chi_{23}\phi_2 + (\chi_{12}-\chi_{13}-\chi_{23})\phi_1 - \kappa_{12}\nabla^2\phi_1 - \kappa_{22}\nabla^2\phi_2\Bigg]\Bigg\},\end{aligned} \tag{2.10}$$

as expected from literature [26].

2.3 Pseudo-spectral methods

The dynamic equations written in the form of (2.9) can be analysed in the spectral representation [28], which describes the problem in the Fourier space.This representation is particularly convenient on a periodic domain, as adopted in our study.

Specifically, we can consider basis functions for square-integrable real-valued functions in $L^2(\Omega)$. Periodic boundary conditions provide a convenient means to model systems with conservation laws, e.g. of components' concentrations. Therefore, we can consider an orthonormal basis $\{e_{\boldsymbol{j}}\}_{\boldsymbol{j}\in\mathbb{Z}^d}$ for periodic functions defined on the domain Ω. Let us denote with $\langle\cdot,\cdot\rangle$ the standard inner product in $L^2(\Omega)$, i.e. the map such that for each $g, h \in L^2(\Omega)$

$$\langle g, h\rangle = \int_\Omega gh.$$

For any scalar field $\phi(\boldsymbol{x}, t)$ defined on the periodic domain Ω and parametrized by the temporal variable, there exist some functions $\widehat{\phi}_{\boldsymbol{j}} : \mathbb{R}_+ \to \mathbb{R}$ taking values on the time interval $\mathbb{R}_+$, such that

$$\phi(\boldsymbol{x}, t) = \sum_{\boldsymbol{j}\in\mathbb{Z}^d} \widehat{\phi}_{\boldsymbol{j}}(t)e_{\boldsymbol{j}}(\boldsymbol{x}) \qquad \forall(\boldsymbol{x}, t) \in \Omega\times\mathbb{R}_+.$$

In other words, ϕ can be decomposed in terms of some coefficients, with respect to a fixed, time-independent basis $\{e_{\boldsymbol{j}}\}_{\boldsymbol{j}\in\mathbb{Z}^d}$. Moreover, the functions $\widehat{\phi}_{\boldsymbol{j}}$ represent the volume fraction ϕ in Fourier space and are uniquely determined by

$$\widehat{\phi}_{\boldsymbol{j}} = \langle\phi, e_{\boldsymbol{j}}\rangle.$$

Indeed, to prove that such functions represent ϕ, let us recall that by orthonormality of the basis $\{e_{\boldsymbol{j}}\}_{\boldsymbol{j}\in\mathbb{Z}^d}$ we have $\langle e_{\boldsymbol{j}}, e_{\boldsymbol{k}}\rangle = \delta_{\boldsymbol{jk}}$, where $\delta_{\boldsymbol{jk}}$ is a multidimensional Kronecker symbol such that

$$\delta_{\boldsymbol{jk}} = \delta_{j_1 k_1} \cdots \delta_{j_d k_d} = \begin{cases} 1 & \text{if } j_1 = k_1, \dots, j_d = k_d, \\ 0 & \text{otherwise.} \end{cases}$$

Then, by linearity of the inner product, we get an explicit form for the coefficients $\widehat{\phi}_{\boldsymbol{j}}$, as

$$\langle \phi, e_{\boldsymbol{j}} \rangle = \sum_{\boldsymbol{k} \in \mathbb{Z}^d} \widehat{\phi}_{\boldsymbol{k}} \langle e_{\boldsymbol{k}}, e_{\boldsymbol{j}} \rangle = \sum_{\boldsymbol{k} \in \mathbb{Z}^d} \widehat{\phi}_{\boldsymbol{k}} \delta_{\boldsymbol{jk}} = \widehat{\phi}_{\boldsymbol{j}}.$$

The representation of a volume fraction ϕ in Fourier space involves a countably infinite number of degrees of freedom, meaning that a full specification of ϕ requires infinitely many degrees of freedom.

However, in this context, experimental data provide only the average volume fraction ϕ evaluated over a finite number of identical d-dimensional hyperrectangular elements, that collectively cover the domain Ω. These average values $\phi_{\boldsymbol{m}}$ can be also considered as the value of ϕ at the center $(x_{1,m_1}, \dots, x_{d,m_d})$ of each element, i.e. $\phi_{\boldsymbol{m}} = \phi(x_{1,m_1}, \dots, x_{d,m_d}, t)$ at a certain time t. Therefore, to get an approximation of ϕ, we need to interpolate between these points $\{(x_{1,m_1}, \dots, x_{d,m_d}), \phi_{\boldsymbol{m}}\}_{\boldsymbol{m} \in \boldsymbol{M}}$, where $\boldsymbol{M}$ denotes the set of indices that identifies the center of each element.

Spectral approximation on a one-dimensional domain In order to clarify the idea of function approximation by its truncated Fourier series on in a d-dimensional domain, we illustrate here the simplest case—$L^2(\mathcal{I})$-integrable one-dimensional functions on a finite interval $\mathcal{I} = [0, L] \subset \mathbb{R}$. For any periodic square-integrable function g there exist some coefficients $\widehat{g}_i$ such that

$$g(x) = \sum_{i \in \mathbb{Z}} \widehat{g}_i e_i(x),$$

where $\{e_i\}_{i \in \mathbb{Z}}$ is the orthonormal basis set for periodic functions in $L^2(\mathcal{I})$.

Suppose now that we have limited information about g and seek to reconstruct an approximation $\widetilde{g}$. Specifically, we assume that the available information consists of the values g_m of g at certain points x_m, for $m = 1, \dots, M$, meaning that we know $g_m = g(x_m)$. Furthermore, we assume that the nodes x_m correspond to the centers of the cells in an equidistant grid over the interval $\mathcal{I}$, such that

$$x_1 \equiv \frac{1}{2}dx < x_2 \equiv \frac{3}{2}dx < \cdots < x_M \equiv \frac{2M-1}{2}dx,$$

where $dx = \frac{L}{M}$ and, in general, $x_m = \frac{2m-1}{2}dx$ for $m = 1, \dots, M$. A possible approach to define the approximation $\widetilde{g}$ is to project g onto a subspace of $\overline{\operatorname{span}\{e_i\}_{i \in \mathbb{Z}}}$. To achieve this, we can choose a suitable basis $\{e_i\}_{i \in \mathbb{Z}}$ so that most of the information about g is concentrated in a few modes. Then, we can apply a low-pass filter to eliminate the modes associated with higher frequencies, so that the approximation of g can be written as a finite sum of M terms, defining the set $I \subset \mathbb{Z}$ of the retained indices, associated with M modes that focus the information.

For instance, let us consider the following orthonormal basis

$$e_i(x) = \begin{cases} \frac{1}{\sqrt{L}} & \text{if } i = 0 \\ \sqrt{\frac{2}{L}} \cos\left(\frac{2\pi}{L} i x\right) & \text{if } i > 0 \\ -\sqrt{\frac{2}{L}} \sin\left(\frac{2\pi}{L} i x\right) & \text{if } i < 0 \end{cases}$$

Let $I = \left\{ -\left\lfloor \frac{M}{2} \right\rfloor, -\left\lfloor \frac{M}{2} \right\rfloor + 1, \ldots, \left\lfloor \frac{M-1}{2} \right\rfloor \right\}$ be the set of M retained indices, associated with the modes that focus the information. Consider now the truncated basis function set $\{e_i\}_{i \in I}$. This new set of functions is a basis for the subspace $\operatorname{span}\{e_i\}_{i \in I}$ where the higher order modes are eliminated, but the construction procedure used to define this set does not ensure orthonormality. However, we can construct an orthonormal basis for the subspace $\operatorname{span}\{e_i\}_{i \in I}$, for instance by applying the Gram-Schmidt algorithm. The process of building an orthonormal basis for $\operatorname{span}\{e_i\}_{i \in I}$ reduces to slightly modify of the basis functions e_i for $i \in I$. For the sake of simplicity, we redefine e_i with a little abuse of notation, so that in the following they denote the modified orthonormal basis functions for the subspace $\operatorname{span}\{e_i\}_{i \in I}$, where

$$e_i(x) = \begin{cases} \frac{1}{\sqrt{L}} & \text{if } i = 0 \\ \sqrt{\frac{2}{L}} \cos\left(\frac{2\pi}{L} i x\right) & \text{if } i > 0 \\ -\sqrt{\frac{2}{L}} \sin\left(\frac{2\pi}{L} i x\right) \zeta_{iM} & \text{if } i < 0 \end{cases} \qquad \text{where} \quad \zeta_{iM} = \begin{cases} \frac{1}{\sqrt{2}} & \text{if } M \text{ even, } i = -\frac{M}{2} \\ 1 & \text{o/w} \end{cases}$$

Finally, the spectral approximation of g is given by

$$\widetilde{g}(x) := \sum_{i \in I} \widehat{g}_i e_i(x),$$

where the coefficients $\widehat{g}_i$ are computed as an approximation of the inner product

$$\langle g, e_i \rangle = \int_{\mathcal{I}} g(x) e_i(x) \, dx.$$

Under the assumption that g is periodic and noting that, by definition, e_i is also periodic on the interval $\mathcal{I}$, the integrand remains periodic. Consequently, following the spectral collocation approach [28], Fourier periodic integration simplifies to the periodic trapezoidal rule. Therefore, we define the coefficients as

$$\widehat{g}_i := dx \sum_{m=1}^{M} g(x_m) e_i(x_m).$$

Spectral approximation on a two-dimensional domain The generalization of the spectral approximation procedure for a space $\Omega \subset \mathbb{R}^2$ is straightforward and will help to clarify the most general case of a d-dimensional domain. Let us assume that the space domain Ω can be written as a Cartesian product of two intervals $\mathcal{I}_r = [0, L_r]$ for $r = 1{,}2$, so that $\Omega = [0, L_1] \times [0, L_2]$. Then, consider for each dimension $r = 1{,}2$ the orthonormal basis $\{e_i^{(r)}\}_{i\in\mathbb{Z}}$ for periodic functions on $\mathcal{I}_r$, such that

$$e_i^{(r)}(x) = \begin{cases} \frac{1}{\sqrt{L_r}} & \text{if } i = 0 \\ \sqrt{\frac{2}{L_r}} \cos\left(\frac{2\pi}{L_r} ix\right) & \text{if } i > 0 \\ -\sqrt{\frac{2}{L_r}} \sin\left(\frac{2\pi}{L_r} ix\right) & \text{if } i < 0 \end{cases}$$

Therefore, an orthonormal basis for periodic functions on Ω is given by $\{e_{ij}\}_{(i,j)\in\mathbb{Z}^2}$, where the functions are defined as tensor products of all the combinations of $e_i^{(r)}$ for $r = 1{,}2$ and $i \in \mathbb{Z}$. In other words, we have $e_{ij} = e_i^{(1)} \otimes e_j^{(2)}$ or equivalently

$$e_{ij}(x, y) = e_i(x)e_j(y) \qquad \forall (x, y) \in \Omega = \mathcal{I}_1 \times \mathcal{I}_2.$$

Indeed, one can easily see that orthonormality holds, performing a direct computation

$$\langle e_{ij}, e_{kl}\rangle = \int_\Omega e_{ij}e_{kl} = \left(\int_0^{L_1} e_i^{(1)} e_k^{(1)}\right)\left(\int_0^{L_2} e_j^{(2)} e_l^{(2)}\right) = \delta_{ik}\delta_{jl}.$$

Consider now a Cartesian grid on Ω made up of $M = M_1M_2$ identical rectangular elements of area v. Each element in the grid can be identified with the corresponding center $\boldsymbol{x}_{mn}$ such that $\boldsymbol{x}_{mn} = (x_m, y_n)$, with $x_m = \frac{2m-1}{2}$ for $m = 1, \dots, M_1$ and $y_n = \frac{2n-1}{2}$ for $n = 1, \dots, M_2$. In a similar way with respect to the one-dimensional case, we introduce the set J, that contains multi-indices $\boldsymbol{j} = (i, j)$ associated with low frequencies modes of the basis $\{e_{ij}\}_{(i,j)\in\mathbb{Z}^2}$. A possible way to easily define J is by considering the sets

$$I_r = \left\{-\left\lfloor\frac{M_r}{2}\right\rfloor, -\left\lfloor\frac{M_r}{2}\right\rfloor + 1, \dots, \left\lfloor\frac{M_r - 1}{2}\right\rfloor\right\} \qquad r = 1{,}2. \tag{2.11}$$

Then, the set of multi-indices J can be written as the Cartesian product $J := I_1 \times I_2$. Moreover, for simplicity, we redefine the set $\{e_{ij}\}_{(i,j)\in J}$ so that it is an orthonormal basis for the subspace $\operatorname{span}\{e_{ij}\}_{(i,j)\in J}$, resulting in $e_{ij} = e_i^{(1)} \otimes e_j^{(2)}$ with

$$e_i^{(r)}(x) = \begin{cases} \frac{1}{\sqrt{L_r}} & \text{if } i = 0 \\ \sqrt{\frac{2}{L_r}} \cos\left(\frac{2\pi}{L_r} ix\right) & \text{if } i > 0 \\ -\sqrt{\frac{2}{L_r}} \sin\left(\frac{2\pi}{L_r} ix\right) \zeta_{iM}^{(r)} & \text{if } i < 0 \end{cases} \tag{2.12}$$

where

$$\zeta_{iM}^{(r)} = \begin{cases} \frac{1}{\sqrt{2}} & \text{if } M_r \text{ even, } i = -\frac{M_r}{2} \\ 1 & \text{o/w} \end{cases}$$

for $r = 1{,}2$ and $i \in I_r$.

Finally, we can define the spectral approximation of a periodic function g on Ω as

$$\widetilde{g}(\boldsymbol{x}) = \sum_{(i,j)\in J} \widehat{g}_{ij} e_{ij}(\boldsymbol{x}),$$

where the coefficients $\widehat{g}_{ij}$ are computed as approximation of the inner product

$$\langle g, e_{ij} \rangle = \int_{\Omega} g(\boldsymbol{x}) e_{ij}(\boldsymbol{x}) \, d\boldsymbol{x}.$$

Once again using the spectral collocation approach, we define these coefficients as

$$\begin{aligned} \widehat{g}_{ij} &:= v \sum_{m=1}^{M_1} \sum_{n=1}^{M_2} g(x_m, y_n) e_{ij}(x_m, y_n) \\ &= dx \, dy \sum_{m=1}^{M_1} \sum_{n=1}^{M_2} g(x_m, y_n) e_i^{(1)}(x_m) e_j^{(2)}(y_n). \end{aligned}$$

For the sake of simplicity, in the following we assume that each function g considered belongs to the subspace $\operatorname{span}\{e_{ij}\}_{(i,j)\in J}$, so that its approximation exactly coincide with itself, i.e. $\widetilde{g} = g$. Furthermore, we denote with $\mathfrak{F}$ the analysis operator that maps functions in $\operatorname{span}\{e_{ij}\}_{(i,j)\in J}$ to their coefficients in the spectral approximation, such that

$$\mathfrak{F} : g \in \operatorname{span}\{e_{ij}\}_{(i,j)\in J} \mapsto \{\widehat{g}_{ij} = \langle g, e_{ij} \rangle\}_{(i,j)\in J}.$$

Then, the synthesis operator is defined as

$$\mathfrak{F}^* : \{\widehat{g}_{ij}\}_{(i,j)\in J} \mapsto g = \sum_{(i,j)\in J} \widehat{g}_{ij} e_{ij}$$

and coincides with the inverse of $\mathfrak{F}$, i.e. $\mathfrak{F}^* = \mathfrak{F}^{-1}$, since by hypothesis $g \in \operatorname{span}\{e_{ij}\}_{(i,j)\in J}$.

2.4 Numerical methods

The procedure illustrated in Section 2.3 provides us a way to describe the field $\phi(\boldsymbol{x}, t)$ of any volume fraction at a time t in an approximation subspace. The dynamic equations (2.9) can then be written in terms of the spectral approximation by substituting the approximated fields ϕ_a into the equations or, equivalently, by projecting such equations onto the approximation subspace.

Let $\Omega \subset \mathbb{R}^d$ be the space domain and suppose to divide into identical elementary volumes $\omega(\boldsymbol{x})$ uniquely identified by their center $\boldsymbol{x}$. Inside each element $\omega(\boldsymbol{x})$ the presence of the mixture can be interpreted with the coexistence of C regions of space, each one uniquely associated with one component of the system. Since we assumed that the mixture occupies the entire domain, each element $\omega(\boldsymbol{x})$ can be written as the disjoint union of the regions $\omega_a(\boldsymbol{x})$ for $a \in \mathcal{A}$, that correspond to the portions of space in $\omega(\boldsymbol{x})$ uniquely associated with the component a, so that $\omega(\boldsymbol{x}) = \bigsqcup_{a\in\mathcal{A}} \omega_a(\boldsymbol{x}, t)$. The underlying assumption in this interpretation is the impossibility for the components to overlap and the presence of harsh bounds between them. However, this has to happen inside an element $\omega(\boldsymbol{x})$, therefore, assuming that the available information on the system is averaged on each element, what we really observe is a coarser picture where the hypothesis on the overlapping of components can be relaxed and volume fractions can be well defined.

The volume occupied by the component $a \in \mathcal{A}$ in the element $\omega(\boldsymbol{x})$ is

$$|\omega_a(\boldsymbol{x},t)| = \int_{\omega(\boldsymbol{x})} \mathbb{1}_{\omega_a(\boldsymbol{x},t)}(\boldsymbol{y})\, d\boldsymbol{y} = \int_{\omega_a(\boldsymbol{x},t)} d\boldsymbol{y},$$

where $\mathbb{1}_{\omega_a(\boldsymbol{x},t)}$ denotes the indicator function of the set $\omega_a(\boldsymbol{x},t)$. On the other hand, assuming that the elements $\omega(\boldsymbol{x})$ are identical, the total volume of each element is

$$\omega := |\omega(\boldsymbol{x})| = \sum_{a\in\mathcal{A}} |\omega_a(\boldsymbol{x},t)|.$$

Therefore, the volume fraction [9] of the component $a \in \mathcal{A}$ can be defined as functions $\phi_a : \Omega \times \mathbb{R}_+ \to [0,1]$ such that

$$\phi_a(\boldsymbol{x},t) = \frac{\omega_a(\boldsymbol{x},t)}{\omega}.$$

Specifically, in what follows, we assume that the domain Ω is partitioned by an equidistant grid into M identical elements $\omega(\boldsymbol{x}) \in \mathbb{R}^d$—intervals, pixels, or voxels for $d = 1,2,3$ respectively—identified by the positions of their centroids $\boldsymbol{x}$. Fluctuations of empty space between individual molecules are assumed negligible relative to the volume ω.

2.4.1 Configuration of the system in the spectral space

Inspired by the approach followed in Section 2.3 for one and two-dimensional domains, we construct an approximation for each volume fraction field $\phi_a(\boldsymbol{x},t)$ with $a \in \mathcal{A}_C$ at a time t. In order to do so, let us recall that the space domain Ω is assumed to be subdivided into M identical elements $\omega(\boldsymbol{x})$ of volume ω and suppose that Ω is a d-dimensional hyperrectangle that can be expressed as a Cartesian product

$$\Omega = \prod_{r=1}^{d} \mathcal{I}_r,$$

of d intervals $\mathcal{I}_r := [0, L_r]$ for $r = 1,\dots,d$. Furthermore, let us consider a midpoint discretization in M_r nodes of each interval $\mathcal{I}_r$ such that

$$x_{r,m_r} = \frac{2m_r - 1}{2} dx_r \quad \text{for } m_r = 1,\dots,M_r,$$

where $dx_r = \frac{L_r}{M_r}$, while the first index of x_{r,m_r} denotes the interval associated with the node and the second index denotes the point in the one-dimensional discretization.

Then, we can easily define a decomposition of the domain Ω into identical elements, by taking the points $(x_{1,m_1},\dots,x_{d,m_d}) \in \Omega$ as their centers. Notice that we have $M = \prod_{r=1}^{d} M_r$ points and, for sake of simplicity, we can denote one with $\boldsymbol{x}_{m_1,\dots,m_d}$ the point $(x_{1,m_1},\dots,x_{d,m_d})$. Moreover, for a shorter notation, we can introduce M multi-indices

$$\boldsymbol{m} = (m_1,\dots,m_d) \in \boldsymbol{M} := \left(\prod_{r=1}^{d} \{1,\dots,M_r\}\right),$$

given by all the possible ordered combinations of m_r, so that $\boldsymbol{x_m} = \boldsymbol{x}_{m_1,\dots,m_d}$ [1].

In other words, the domain Ω is subdivided into M identical smaller hyperrectangles $\omega(\boldsymbol{x_m})$, with $\boldsymbol{m} \in \boldsymbol{M}$, where $\boldsymbol{x_m}$ is the center of the element $\omega(\boldsymbol{x_m})$ and coincides with one of the points of the midpoint grid.

Consider the orthonormal basis $\{e_i^{(r)}\}_{i\in I_r}$ for approximated periodic functions on the interval $\mathcal{I}_r$ for each $r = 1\dots,d$, where I_r is given by (2.11), while $e_i^{(r)}$ is defined as in (2.12) and denotes the basis function of the subspace where we have already cut the modes associated with higher frequencies.

Then, let us define the set J of multi-indices as the Cartesian product $J = \prod_{r=1}^d I_r$, so that elements of J are multi-indices $\boldsymbol{j} = (j_1,\dots,j_d)$ with $j_r \in I_r$ for $r = 1,\dots,d$. Therefore, we can define a basis for approximated periodic functions on Ω as $\{e_{\boldsymbol{j}}\}_{\boldsymbol{j}\in J}$, where

$$e_{\boldsymbol{j}} = e_{j_1}^{(1)} \otimes \cdots \otimes e_{j_d}^{(d)}. \tag{2.13}$$

Finally, at each fixed time t, volume fraction fields $\phi_a(\boldsymbol{x},t)$ of each component $a \in \mathcal{A}_C$ can be approximated in the subspace $\operatorname{span}\{e_{\boldsymbol{j}}\}_{\boldsymbol{j}\in J}$ as

$$\begin{aligned}\phi_a(\boldsymbol{x},t) \simeq \widetilde{\phi}_a(\boldsymbol{x},t) &= \sum_{\boldsymbol{j}\in J} \widehat{\phi}_{a,\boldsymbol{j}}(t) e_{\boldsymbol{j}}(\boldsymbol{x}) \\ &= \sum_{\boldsymbol{j}\in J} \left[\widehat{\phi}_{a,\boldsymbol{j}}(t) \prod_{r=1}^d e_{j_r}^{(r)}(x_r)\right],\end{aligned} \tag{2.14}$$

where x_r denotes a the r^{th} component of a vector variable $\boldsymbol{x} \in \Omega \subset \mathbb{R}^d$ and the coefficients of the decomposition are given by the approximation of the inner product $\langle \phi_a, e_{\boldsymbol{j}}\rangle$, according to the spectral collocation approach

$$\begin{aligned}\widehat{\phi}_{a,\boldsymbol{j}} :&= \omega \sum_{m\in \boldsymbol{M}} \phi_a(\boldsymbol{x_m},t) e_{\boldsymbol{j}}(\boldsymbol{x_m}) \\ &= \omega \sum_{m_1=1}^{M_1} \cdots \sum_{m_d=1}^{M_d} \left[\phi_a(x_{1,m_1},\dots,x_{d,m_d},t) \prod_{r=1}^d e_{j_r}^{(r)}(x_{r,m_r})\right],\end{aligned}$$

where $\omega = |\omega(\boldsymbol{x_m})|$ is the measure of the element $\omega(\boldsymbol{x_m})$, independent of the center $\boldsymbol{x_m}$ and given by $\omega = \prod_{r=1}^d dx_r$.

Notice that, in general the approximation $\widetilde{\phi}_a(\boldsymbol{x},t)$ is well distinct from the real scalar field $\phi_a(\boldsymbol{x},t)$. However, for the sake of simplicity, in the following we identify the approximation $\widetilde{\phi}_a(\boldsymbol{x},t)$ with the original field, assuming that only small errors are introduced through the projection onto the Fourier space and the cut of higher order frequencies. In other words, we imagine that each field $\phi(\boldsymbol{x},t)$ is a function in $\operatorname{span}\{e_{\boldsymbol{j}}\}_{\boldsymbol{j}\in J}$ so that the approximation coincides with the real field.

---

[1] An alternative approach would be to introduce an ordering rule over the set of points of the discretization $\{(x_{1,m_1},\dots,x_{d,m_d})\}_{m_r\in\{1,\dots,M_r\},\, r\in\{1,\dots,d\}}$. In such manner, we can denote with $\boldsymbol{x}_m$ the m^{th} center for $m = 1,\dots,M$. Specifically, we are introducing a bijection $\rho : \{1,\dots,M\} \to \{1,\dots,d\} \times \{1,\dots,M_d\}$ and denoting $\boldsymbol{x}_m = (x_{\rho(m)},\dots,x_{d,\rho(m)})$.

Moreover, we introduce the analysis $\mathfrak{F}$ operator such that

$$\mathfrak{F}\phi_a = \left\{\widehat{\phi}_{a,\boldsymbol{j}} = \langle \phi_a, e_{\boldsymbol{j}} \rangle\right\}_{\boldsymbol{j}\in \boldsymbol{J}}.$$

On the other hand, by hypothesis on the domain of $\mathfrak{F}$, the synthesis operator $\mathfrak{F}^*$ coincides with the inverse of $\mathfrak{F}$, so that $\mathfrak{F}^* = \mathfrak{F}^{-1}$ and

$$\mathfrak{F}^*\{\widehat{\phi}_{a,\boldsymbol{j}}\}_{\boldsymbol{j}\in J} = \sum_{\boldsymbol{j}\in J} \widehat{\phi}_{a,\boldsymbol{j}} e_{\boldsymbol{j}}.$$

2.4.2 Projection of the dynamical equations

Let us consider the dynamic equations (2.9) and assume for simplicity that the coefficient Λ is a positive constant. In order to project these onto the approximation subspace $\operatorname{span}\{e_{\boldsymbol{j}}\}_{\boldsymbol{j}\in J}$, let us first denote the derivative of $\widehat{\phi}_{ij}$ with respect to the time variable, as $\dot{\widehat{\phi}}_{\boldsymbol{j}}$ for $\boldsymbol{j} \in J$. On the other hand, we denote the derivative of $e_i^{(d)}$ with respect to the space variable as $\left(e_i^{(r)}\right)'$. Notice that for each one-dimensional basis function $e_i^{(r)}$ we have

$$\begin{aligned}\left(e_i^{(r)}\right)' &= -\frac{2\pi i}{L_r} e_{-i}^{(r)},\\ \left(e_i^{(r)}\right)'' &= -(2\pi)^2 \left(\frac{i}{L_r}\right)^2 e_i^{(r)}.\end{aligned}$$

Therefore, it also holds

$$\nabla^2 e_{\boldsymbol{j}} = -(2\pi)^2 \left(\sum_{r=1}^{d} \frac{j_r^2}{L_r^2}\right) e_{\boldsymbol{j}},$$

where we can denote for simplicity the coefficient that appears from the derivation as $g_{\boldsymbol{j}} = -(2\pi)^2 \left(\sum_{r=1}^{d} \frac{j_r^2}{L_r^2}\right)$ for $(i, j) \in J$, so that the laplacian of the basis functions can be also written as $\nabla^2 e_{\boldsymbol{j}} = g_{\boldsymbol{j}} e_{\boldsymbol{j}}$.

Projecting the dynamic equations term by term onto the approximation subspace, we have that, by linearity of the inner product, the left hand side of the dynamical equation becomes

$$\begin{aligned}\langle \partial_t \phi_a, e_{\boldsymbol{j}} \rangle &= \left\langle \sum_{\boldsymbol{k}\in J} \dot{\widehat{\phi}}_{a,\boldsymbol{k}} e_{\boldsymbol{k}}, e_{\boldsymbol{j}} \right\rangle = \sum_{\boldsymbol{k}\in J} \dot{\widehat{\phi}}_{a,\boldsymbol{k}} \langle e_{\boldsymbol{k}}, e_{\boldsymbol{j}} \rangle\\ &= \sum_{\boldsymbol{k}\in J} \dot{\widehat{\phi}}_{a,\boldsymbol{k}} \delta_{\boldsymbol{j}\boldsymbol{k}} = \dot{\widehat{\phi}}_{a,\boldsymbol{j}}.\end{aligned}$$

On the other hand, recalling that by definition of $g_{\boldsymbol{j}}$, we have $\nabla^2 e_{\boldsymbol{j}} = g_{\boldsymbol{j}} e_{\boldsymbol{j}}$, the last two terms of the right hand side give

$$\begin{aligned}
\langle \nabla^2 \phi_a, e_{\boldsymbol{j}} \rangle &= \sum_{\boldsymbol{k}\in J} \widehat{\phi}_{a,\boldsymbol{k}} \langle \nabla^2 e_{\boldsymbol{k}}, e_{\boldsymbol{j}} \rangle = \sum_{\boldsymbol{k}\in J} g_{\boldsymbol{k}} \widehat{\phi}_{a,\boldsymbol{k}} \langle e_{\boldsymbol{k}}, e_{\boldsymbol{j}} \rangle \\
&= \sum_{\boldsymbol{k}\in J} g_{\boldsymbol{k}} \widehat{\phi}_{a,\boldsymbol{k}} \delta_{\boldsymbol{jk}} = g_{\boldsymbol{j}} \widehat{\phi}_{a,\boldsymbol{j}}, \\
\langle \nabla^4 \phi_a, e_{\boldsymbol{j}} \rangle &= \sum_{\boldsymbol{k}\in J} \widehat{\phi}_{a,\boldsymbol{k}} \langle \nabla^4 e_{\boldsymbol{k}}, e_{\boldsymbol{j}} \rangle = \sum_{\boldsymbol{k}\in J} \widehat{\phi}_{a,\boldsymbol{k}} \left\langle \nabla^2 \left(\nabla^2 e_{\boldsymbol{k}} \right), e_{\boldsymbol{j}} \right\rangle \\
&= \sum_{\boldsymbol{k}\in J} g_{\boldsymbol{k}} \widehat{\phi}_{a,\boldsymbol{k}} \left\langle \nabla^2 e_{\boldsymbol{k}}, e_{\boldsymbol{j}} \right\rangle = \sum_{\boldsymbol{k}\in J} g_{\boldsymbol{k}}^2 \widehat{\phi}_{a,\boldsymbol{k}} \langle e_{\boldsymbol{k}}, e_{\boldsymbol{j}} \rangle = \\
&= \sum_{\boldsymbol{k}\in J} g_{\boldsymbol{k}}^2 \widehat{\phi}_{a,\boldsymbol{k}} \delta_{\boldsymbol{jk}} = g_{\boldsymbol{j}}^2 \widehat{\phi}_{a,\boldsymbol{j}}.
\end{aligned}$$

Finally, the logarithmic terms can be treated through Green's identities and using periodic boundary conditions to get rid of boundary terms. Introducing the outward pointing unit normal $\boldsymbol{N}$ to the surface element, we have

$$\begin{aligned}
\langle \nabla^2 \log \phi_a, e_{\boldsymbol{j}} \rangle &= \int_\Omega \nabla^2 \left(\log \phi_a \right) e_{\boldsymbol{j}} = \int_{\partial\Omega} \nabla \left(\log \phi_a \right) e_{\boldsymbol{j}} \cdot \boldsymbol{N} - \int_\Omega \nabla \log \phi_a \cdot \nabla e_{\boldsymbol{j}} \\
&= - \int_\Omega \nabla \log \phi_a \cdot \nabla e_{\boldsymbol{j}} = - \int_{\partial\Omega} \left(\log \phi_a \right) \nabla e_{\boldsymbol{j}} \cdot \boldsymbol{N} + \int_\Omega \left(\log \phi_a \right) \nabla^2 e_{\boldsymbol{j}} \\
&= \int_\Omega \left(\log \phi_a \right) \nabla^2 e_{\boldsymbol{j}} = \langle \log \phi_a, \nabla^2 e_{\boldsymbol{j}} \rangle = g_{\boldsymbol{j}} \langle \log \phi_a, e_{\boldsymbol{j}} \rangle.
\end{aligned}$$

The projections of the dynamic equations can now be written as a set of $(C-1)M$ ordinary differential equations in terms of the sets of functions $\widehat{\phi}_a = \left\{ \widehat{\phi}_{a,\boldsymbol{j}} = \widehat{\phi}_{a,\boldsymbol{j}}(t) \right\}_{\boldsymbol{j}\in J}$ for $a \in \mathcal{A}_C$, that are the coefficients of the spectral approximation (2.14). Therefore, we have that the evolution of $\widehat{\phi}_a$ for $a \in \mathcal{A}_C$ is described for each $\boldsymbol{j} \in J$, by

$$\begin{aligned}
\dot{\widehat{\phi}}_{a,\boldsymbol{j}} = \Lambda \Bigg[g_{\boldsymbol{j}} \left\langle \frac{\log \left(\mathfrak{F}^* \widehat{\phi}_a \right)}{N_a} - \frac{\log \left(1 - \sum_{b\in\mathcal{A}_C} \mathfrak{F}^* \widehat{\phi}_b \right)}{N_B}, e_{\boldsymbol{j}} \right\rangle \\
+ \sum_{b\in\mathcal{A}_C} \left(\chi_{ab} - \chi_{bC} - \chi_{aC} \right) g_{\boldsymbol{j}} \widehat{\phi}_{b,\boldsymbol{j}} - \sum_{b\in\mathcal{A}_C} \kappa_{ab} g_{\boldsymbol{j}}^2 \widehat{\phi}_{b,\boldsymbol{j}} \Bigg].
\end{aligned} \tag{2.15}$$

2.5 Numerical integration scheme

To simulate the dynamics of the system, specifically the evolution of volume fractions, we numerically integrate the governing partial differential equations over time. The goal is to obtain phase separated configurations, which represent equilibrium states, when appropriate parameters are chosen.

In this Section, we explore two possible approaches. The first method relies on the open-source `Python` module `py-pde` [34], which provides tools for solving partial differential equations using the method of lines. This method discretizes spatial derivatives using a finite difference scheme while employing standard numerical methods for time integration of the resulting system of ordinary differential equations. The second approach focuses on solving the system of differential equations derived from the application of spectral methods, as formulated in (2.15). In this case, the evolution equations are integrated directly in spectral space using a simple explicit Euler scheme, which offers a straightforward way to advance the system in time.

2.5.1 Finite difference discretization

The `py-pde` module is an open-source `Python` library deigned for solving partial differential equations, using the method of lines. The principles behind this technique is the discretization of all spatial dimensions, that are integrated using finite difference methods to write differential operators. This reduces a partial differential equation to a system of ordinary differential equation, that can be solved applying of standard methods, such as forward Euler, Crank-Nicolson or explicit Adams-Bashforth.

As before, let us suppose for simplicity that the domain Ω is a d-dimensional hyperrectangle, that can be expressed as a Cartesian product of d intervals $\mathcal{I}_r = [0, L_r]$ for $r = 1, \dots, d$, such that $\Omega = \prod_{r=1}^{d} \mathcal{I}_r$.

Moreover, we assume that the volume fractions ϕ_a satisfy periodic boundary conditions, so that the mathematical problem for the evolution of ϕ_a can be written combining the set of $C-1$ equations (2.9) in $\Omega \times \mathbb{R}_+$ for $a \in \mathcal{A}_C$, along with the following conditions

$$\begin{cases} \phi_a|_{x_r=0} = \phi_a|_{x_r=L_r} & \text{for } r = 1, \dots, d \\ \phi_a(\boldsymbol{x}, 0) = \phi_a^{(0)}(\boldsymbol{x}) & \forall \boldsymbol{x} \in \Omega \end{cases}$$

where $\phi^{(0)}$ is the initial state of the system and satisfies

$$0 \le \phi_a^{(0)} \le 1,$$
$$\sum_{a \in \mathcal{A}_C} \phi_a^{(0)} \le 1,$$

so that it represents a proper volume fraction for the first $C-1$ components of the mixture and it is possible to define the scalar field associated with the volume fraction of the last component as $\phi_C^{(0)} = 1 - \sum_{a \in \mathcal{A}_C} \phi_a^{(0)}$, so that it satisfies as well the constraint $0 \le \phi_C^{(0)} \le 1$.

Introducing discretization of the space as described in Sec. 2.4.1, the generation of the initial state can proceed as follows. Suppose that the initial state of the component $a \in \mathcal{A}_C$ can be decomposed as

$$\phi_a^{(0)}(\boldsymbol{x}_{\boldsymbol{m}}) = \langle \phi_a^{(0)} \rangle + \widetilde{\phi}_a^{(0)}(\boldsymbol{x}_{\boldsymbol{m}}) \quad \forall \boldsymbol{m} \in \boldsymbol{M},$$

where $\langle \phi_a^{(0)} \rangle$ is the average volume fraction of a across the domain Ω and $\widetilde{\phi}_a^{(0)}(\boldsymbol{x}_{\boldsymbol{m}})$ is some Gaussian noise depending on the position $\boldsymbol{x}_{\boldsymbol{m}} \in \Omega$. Such noise can be seen at each point $\boldsymbol{x}_{\boldsymbol{m}}$ with $\boldsymbol{m} \in \boldsymbol{M}$, as a realization of a Gaussian random variable distributed according to a normal distribution $\mathcal{N}(0, \sigma_a)$, with mean zero and arbitrary standard deviation $\sigma_a > 0$, such that $\phi_a^{(0)}(\boldsymbol{x_m}) \geq 0$ and for which the mean of $\widetilde{\phi}_a^{(0)}$ over the domain Ω is equal to zero, i.e.

$$\frac{1}{M}\sum_{\boldsymbol{m}\in\boldsymbol{M}} \widetilde{\phi}_a^{(0)}(\boldsymbol{x_m}) = 0,$$

so that the average volume fraction is not influenced by different realizations. In other words, for each realization of the noise, it holds

$$\frac{1}{M}\sum_{\boldsymbol{m}\in\boldsymbol{M}} \phi_a^{(0)}(\boldsymbol{x_m}) = \langle\phi_a^{(0)}\rangle.$$

To generate the state $\phi_a^0(\boldsymbol{x_m})$, we initially set a fixed value for the average volume fraction $\langle\phi_a^{(0)}\rangle$ of component $a \in \mathcal{A}_C$. Then, we generate a Gaussian noise ξ from a random variable $\mathcal{N}(0,\sigma_a)$ and we set

$$\psi_a^{(0)}(\boldsymbol{x_m}) = \langle\phi_a^{(0)}\rangle + \xi.$$

Now, we check that $\psi_a^{(0)}(\boldsymbol{x_m}) \geq 0$ for each $\boldsymbol{m} \in \boldsymbol{M}$, otherwise we need to resample or choose a smaller σ_a. If the condition holds, we rescale the generated value to satisfy the constraint on the average volume fraction, by setting for $a \in \mathcal{A}_C$

$$\phi_a^{(0)}(\boldsymbol{x_m}) = \frac{\langle\phi_a^{(0)}\rangle}{\frac{\omega}{M}\sum_{\boldsymbol{n}\in\boldsymbol{M}} \phi_a^{(0)}(\boldsymbol{x_n})}\psi_a^{(0)}(\boldsymbol{x_m}).$$

Finally, we define $\phi_C^{(0)}(\boldsymbol{x_m}) = 1 - \sum_{\boldsymbol{m}\in\boldsymbol{M}} \phi^{(0)}(\boldsymbol{x_m})$ and we can verify that possible states are generated by checking that

$$\begin{cases} 0 \leq \phi_a^{(0)}(\boldsymbol{x_m}) \leq 1 & \forall a \in \mathcal{A},\ \boldsymbol{m} \in \boldsymbol{M} \\ \sum_{a\in\mathcal{A}} \phi_a^{(0)}(\boldsymbol{x_m}) = 1 & \forall \boldsymbol{m} \in \boldsymbol{M} \\ \frac{1}{M}\sum_{\boldsymbol{m}\in\boldsymbol{M}} \phi_a^{(0)}(\boldsymbol{x_m}) = \langle\phi_a^{(0)}\rangle & \forall a \in \mathcal{A} \end{cases}$$

Once a numerical scheme for solving the dynamic equations is defined, the system can be evolved until it stabilizes. The system will evolve minimizing its free energy, leading to phase separated configurations when appropriate parameters are chosen. In this context, a key aspect is determining when equilibrium has been reached. One way to assess this is by monitoring the time evolution of the free energy. Equilibrium is typically identified when the free energy stabilizes within a predefined tolerance, indicating that further evolution no longer significantly alters the system.

Binary mixture in a two-dimensional domain For the simple case of a thin film of a binary mixture, the problem reduces to the study of a two dimensional domain $\Omega \subset \mathbb{R}^2$. Assuming that Ω is a rectangle in the Euclidean space expressed as $\Omega = [0, L_1] \times [0, L_2]$ and that the diffusion coefficient Λ is a constant, the mathematical problem becomes

$$\begin{cases} \partial_t\phi = \Lambda\nabla^2\left[\frac{\log\phi}{N_1} - \frac{\log(1-\phi)}{N_2} - 2\chi\phi - \kappa\nabla^2\phi\right] & \text{in } \Omega\times\mathbb{R}_+ \\ \phi(x,0,t) = \phi(x, L_2, t) & \forall(x,t) \in [0,L_1]\times\mathbb{R}_+ \\ \phi(0,y,t) = \phi(L_1,y,t) & \forall(y,t) \in [0,L_2]\times\mathbb{R}_+ \\ \phi(x,y,0) = \phi^{(0)}(x,y) & \forall(x,y)\in\Omega \end{cases} \tag{2.16}$$

where we set $\phi := \phi_1$, $\chi := \chi_{12} = \chi_{21}$ and $\kappa := \kappa_{11}$.

To illustrate the arise of phase separation in a binary mixture, we numerically solve the problem with a finite difference discretization in a square domain $\Omega = [0{,}10] \times [0{,}10]$ using parameters that promote phase separation. The evolution of the volume fractions is visualized in Figure 2.1, which shows snapshots of the system at different times. Each snapshot represents the spatial distribution of the mixture components using a colormap.

The simulation is performed over the time interval $[0, T] = [0, 10^6]$ with a time step of $dt = 0.1$ on a uniform grid of 150×150 square cells. The diffusion coefficient is set as $\Lambda = 10^{-5}$. The dynamics is generated for relative sizes $N_1 = N_2 = 1$, interaction parameter $\chi = 4$ and gradient coefficient $\kappa = 0.5$. The initial condition is randomly generated with mean volume fractions $\langle \phi_1^{(0)} \rangle = \langle \phi_2^{(0)} \rangle = 0.5$.

The corresponding free energy evolution, shown in Figure 2.3a, confirms that the system gradually stabilizes as it approaches equilibrium.

Ternary mixtures in a three-dimensional domain For a ternary mixture in a two-dimensional domain Ω, the evolution of volume fractions ϕ_a for $a \in \mathcal{A}_C = \{1{,}2\}$ is governed by (2.10). To validate the model, we aim to reproduce the results described in [20].

Figure 2.2 visualizes the initial and equilibrium states of the volume fractions, obtained by solving the dynamic equations using a finite difference discretization. The parameters are chosen to induce phase separation in a concentric pattern. Each image represents the spatial distribution of the mixture components at a given time, where the volume fractions are mapped to RGB channels, producing an RGB visualization.

The simulation is performed on a uniform 150×150 grid of square cells over the time interval $[0, T] = [0, 10^7]$ with a time step of $dt = 0.1$. The diffusion coefficient Λ is set to 10^{-6}, with relative sizes $N_1 = N_2 = N_3 = 1$, interaction parameters $\chi_{12} = 3$, $\chi_{13} = 6$, $\chi_{23} = 3$ and gradient coefficients $\kappa_{11} = \kappa_{22} = 0.5$, $\kappa_{12} = 0.1$. The initial condition is randomly generated with mean volume fractions $\langle \phi_1^{(0)} \rangle = 0.7$, $\langle \phi_2^{(0)} \rangle = 0.2$, $\langle \phi_3^{(0)} \rangle = 0.1$.

In Figure 2.3b, the corresponding free energy evolution confirms the gradual stabilization of the system, providing a quantitative measure of the relaxation process.

2.5.2 Integration in spectral space

A direct consequence of the reduction of the dynamic equations to a set of ordinary differential equations is the possibility to derive the evolution of the volume fraction ϕ_a through a simple numerical integration scheme.

Indeed, for example in the case of binary mixtures on a two-dimensional domain the mathematical problem (2.16) reduces to the following

$$\begin{cases} \dot{\widehat{\phi}}_{ij} = \Lambda \left[\left\langle \frac{\log\left(\mathfrak{F}^*\widehat{\phi}\right)}{N_1} - \frac{\log\left(1-\mathfrak{F}^*\widehat{\phi}\right)}{N_2}, e_{ij} \right\rangle - 2\chi g_{ij}\widehat{\phi}_{ij} - \kappa g_{ij}^2 \widehat{\phi}_{ij} \right] & \text{in } \mathbb{R}_+ \\ \widehat{\phi}_{ij}(0) = \left(\mathfrak{F}\phi^{(0)}\right)_{ij} \end{cases} \tag{2.17}$$

where the periodic boundary conditions are implicitly taken into account in the spectral decomposition and the initial condition $\left(\mathfrak{F}\phi^{(0)}\right)_{ij}$ is defined through the initial volume fraction distribution $\phi^{(0)}$ such that

$$\phi^{(0)}(\boldsymbol{x}) = \sum_{(i,j)\in J} \widehat{\phi^{(0)}}_{ij} e_{ij}(\boldsymbol{x}).$$

Furthermore, one can notice that the first term on the right hand side can also be written in terms of the analysis operator $\mathfrak{F}$ as

$$\left\{\left\langle \frac{\log\left(\mathfrak{F}^*\widehat{\phi}\right)}{N_1} - \frac{\log\left(1-\mathfrak{F}^*\widehat{\phi}\right)}{N_2}, e_{ij}\right\rangle\right\}_{(i,j)\in J} = \mathfrak{F}\left(\frac{\log\left(\mathfrak{F}^*\widehat{\phi}\right)}{N_1} - \frac{\log\left(1-\mathfrak{F}^*\widehat{\phi}\right)}{N_2}\right).$$

The problem (2.17) can be written in a more compact form by introducing an operator G that acts on the set of modes $\widehat{\phi}$ and gives a set of modes, where each mode $\widehat{\phi}_{ij}$ is multiplied by the corresponding factor g_{ij}, so that

$$G : \widehat{\phi} \mapsto \{g_{ij}\widehat{\phi}_{ij}\}_{(i,j)\in J}.$$

Then, the compact form is

$$\begin{cases} \dot{\widehat{\phi}} = \Lambda\left[\mathfrak{F}\left(\frac{\log\left(\mathfrak{F}^*\widehat{\phi}\right)}{N_1} - \frac{\log\left(1-\mathfrak{F}^*\widehat{\phi}\right)}{N_2}\right) - 2\chi G\widehat{\phi} - \kappa G^2\widehat{\phi}\right] & \text{in } \mathbb{R}_+ \\ \widehat{\phi}(0) = \mathfrak{F}\phi^{(0)} \end{cases}$$

One of the most straightforward integration schemes to numerically solve a set of differential equations is the Euler method. For instance, consider an temporal interval $[0,T] \subset \mathbb{R}_+$ and a discretization of such interval, with time step dt. In other words, we consider the set of instants $t_0 \equiv 0 < t_1 < \cdots < t_N \equiv T$, with $t_{n+1} = t_n + dt$. Let us denote with $h = h(t;\widehat{\phi}(t))$ the right hand side of the differential equations in the compact form, such that

$$h(t;\widehat{\phi}(t)) := \Lambda\left[\mathfrak{F}\left(\frac{\log\left(\mathfrak{F}^*\widehat{\phi}\right)}{N_1} - \frac{\log\left(1-\mathfrak{F}^*\widehat{\phi}\right)}{N_2}\right) - 2\chi G\widehat{\phi} - \kappa G^2\widehat{\phi}\right].$$

Let $\widehat{\phi}^{(n)}$ and $h^{(n)}$ be respectively the approximation of the volume fraction coefficients $\widehat{\phi}$ and the approximation of the right hand side h at a time $t = t_n$, so that $\widehat{\phi}^{(n)} \simeq \widehat{\phi}(t_n)$ and $h^{(n)} \simeq h(t_n;\widehat{\phi}(t_n))$. Choosing the approximation $h^{(n)}$ to be $h^{(n)} := h\left(t_n;\widehat{\phi}^{(n)}\right)$, through the Euler method we have

$$\begin{cases} \widehat{\phi}^{(n+1)} = \widehat{\phi}^{(n)} + dt\, h^{(n)} \\ \widehat{\phi}^{(0)} = \mathfrak{F}\phi^{(0)} \end{cases}$$

that describes the evolution of the coefficients $\widehat{\phi}$ and, therefore, of the volume fraction $\phi(\boldsymbol{x}) = \sum_{(i,j)\in J} \widehat{\phi}_{ij}(t) e_{ij}(\boldsymbol{x})$.

The case binary mixtures can be easily extended to numerically integrate the system of dynamic equations that describe the evolution of a mixture of C components. We denote with $\widehat{\phi} = \{\widehat{\phi}_{a,\boldsymbol{j}}\}_{a\in\mathcal{A}_C,\ \boldsymbol{j}\in J}$ the set of modes and define $h = h(t;\widehat{\phi}(t))$ the right hand side of the dynamic equations (2.15) written in vector form. Introducing an initial state $\phi_a^{(0)}$, such that $\phi_a(\boldsymbol{x},0) = \phi_a^{(0)}(\boldsymbol{x})$ for $a \in \mathcal{A}_C$. Then, the initial condition for the system in Fourier space can be defined projecting the $\phi^{(0)}$ onto the approximation space, so that we can set $\widehat{\phi}(0) = \mathfrak{F}\phi^{(0)}$ and apply the preferred numerical integration scheme to determine the evolution of volume fractions.

2.6 Metropolis-Hastings for equilibrium sampling

While numerical solution of dynamic equations provides the *macroscopic* evolution of the system from an initial state toward equilibrium, in small systems fluctuations may play important role and perturb the system's state. One may account for such fluctuations by introducing noise terms into the equation [5, 26, 33]. An alternative approach relies on the Metropolis-Hastings algorithm [10], which produces statistical samples directly from an equilibrium ensemble, thereby profiting on principles of statistical mechanics.

Here, we assume that that the system follows the canonical ensemble, where the probability density of observing a particular configuration $\boldsymbol{\phi}$, given the vector of parameters $\boldsymbol{\theta}$, is given by the Boltzmann distribution

$$p(\boldsymbol{\phi}|\boldsymbol{\theta}) \propto e^{-\beta F(\boldsymbol{\phi}|\boldsymbol{\theta})}, \tag{2.18}$$

where $F(\boldsymbol{\phi}|\boldsymbol{\theta})$ is the free energy of the system, as expressed in Eq. (2.6) for fixed parameters $\boldsymbol{\theta}$ and $\beta = 1/(k_{\mathrm{B}}T)$ expresses the inverse thermal energy. The parameter vector $\boldsymbol{\theta}$, consists of the interaction parameters χ_{ab}, the gradient coefficients κ_{ab} and molecular sizes N_a arranged in a predefined order. This formulation reflects the thermodynamic principle that lower energy states are more likely to occur in equilibrium while still allowing for fluctuations due to thermal effects.

The Metropolis-Hastings algorithm is based on a Markov chain Monte Carlo sampling process and ensures that the generated configurations correctly follow the objective probability distribution, without the need to explicitly know the normalizing factor, which can be difficult to compute. The algorithm begins with an initial configuration $\boldsymbol{\phi}^{(0)}$, which may be randomly generated or selected from a precomputed equilibrium state. At each step, a candidate configuration $\boldsymbol{\phi}'$ is proposed by applying a small random perturbation to the current configuration $\boldsymbol{\phi}^{(i)}$. The choice of the proposal distribution $q(\boldsymbol{\phi}'|\boldsymbol{\phi}^{(i)})$ plays a crucial role in determining the efficiency of sampling and convergence to equilibrium.

The proposed state is accepted or rejected according to the based on the Metropolis acceptance criterion, which depends on the change in free energy

$$\Delta F = F(\boldsymbol{\phi}'|\boldsymbol{\theta}) - F(\boldsymbol{\phi}^{(i)}|\boldsymbol{\theta}).$$

Then, the acceptance probability is given by

$$p_{\text{accept}}(\boldsymbol{\phi}'|\boldsymbol{\phi}^{(i)}) = \min\left\{1,\ \frac{q(\boldsymbol{\phi}^{(i)}|\boldsymbol{\phi}')}{q(\boldsymbol{\phi}'|\boldsymbol{\phi}^{(i)})} e^{-\beta\Delta F}\right\}. \tag{2.19}$$

If the move is accepted, the configuration is updated as $\boldsymbol{\phi}^{(i+1)} = \boldsymbol{\phi}'$; otherwise the system remains in the previous state and $\boldsymbol{\phi}^{(i+1)} = \boldsymbol{\phi}^{(i)}$. By iterating this process over a sufficiently large number of steps, the algorithm explores the configuration space, eventually producing an ensemble of equilibrium states that correctly sample the Boltzmann distribution (2.18).

2.6.1 Choosing a reversible proposal distribution

The efficiency of the Metropolis-Hastings sampling depends strongly on the choice of the proposal distribution $q(\boldsymbol{\phi}'|\boldsymbol{\phi})$, which determines how new configurations are generated. To ensure proper sampling, the Markov chain must satisfy detailed balance, meaning that, in equilibrium, the probability of transitioning from $\boldsymbol{\phi}$ to $\boldsymbol{\phi}'$ must be the same as transitioning from $\boldsymbol{\phi}'$ to $\boldsymbol{\phi}$, so that

$$p(\boldsymbol{\phi}|\boldsymbol{\theta})q(\boldsymbol{\phi}'|\boldsymbol{\phi})p_{\text{accept}}(\boldsymbol{\phi}'|\boldsymbol{\phi}) = p(\boldsymbol{\phi}'|\boldsymbol{\theta})q(\boldsymbol{\phi}|\boldsymbol{\phi}')p_{\text{accept}}(\boldsymbol{\phi}|\boldsymbol{\phi}').$$

A reversible proposal distribution, which inherently satisfies detailed balance, can be defined using a symmetric proposal, where the probability of proposing a move from $\boldsymbol{\phi}$ to $\boldsymbol{\phi}'$ is equal to the reverse move, so that

$$q(\boldsymbol{\phi}'|\boldsymbol{\phi}) = q(\boldsymbol{\phi}|\boldsymbol{\phi}'). \tag{2.20}$$

This choice cancels out the proposal ratio cancels out in the general acceptance probability (2.19), that is reduced to the simpler form

$$p_{\text{accept}}(\boldsymbol{\phi}'|\boldsymbol{\phi}^{(i)}) = \min\left\{1,\ e^{-\beta\Delta F}\right\}.$$

In this work, we adopt the proposal scheme described in Algorithm 1. To build the candidate configuration, at each step a single site $\bar{m}$ of the discretized domain is selected and all volume fractions at that site are updated. Then, to preserve the average volume fraction of each component across the domain, a global rescaling factor is applied to all other sites.

Algorithm 1 Proposal scheme

```
Require: $\boldsymbol{\phi}$ current vector of $C-1$ volume fractions
Require: $\bar{\phi}_a$ average volume fractions in $\Omega$ for $a \in \mathcal{A}_C$
Ensure: $\bar{\phi}_a = \frac{1}{M}\sum_{\boldsymbol{m}\in\boldsymbol{M}} \phi_a(\boldsymbol{x}_{\boldsymbol{m}})$
    Select a random site $\bar{\boldsymbol{m}} \in \boldsymbol{M}$ from the domain
    Sample $C$ new volume fractions $u_a \sim \mathrm{Dir}(1,\ldots,1)$ that ensures $\sum_{a\in\mathcal{A}} u_a = 1$
    Set: $\phi'_a(\boldsymbol{x}_{\bar{\boldsymbol{m}}}) \leftarrow u_a$
    Set: $\phi'_a(\boldsymbol{x}_{\boldsymbol{m}}) \leftarrow \frac{\boldsymbol{\phi}_a(\boldsymbol{x}_{\boldsymbol{m}})}{\alpha_a}$, with $\alpha_a$ scaling factor, ensuring the preservation of $\bar{\phi}_a$
```

The updated values u_a for $a \in \mathcal{A}$ are sampled from a Dirichlet distribution $\mathrm{Dir}(1,\ldots,1)$. In the special case where all parameters are equal to 1, this distribution reduces to a uniform distribution over the space where $u_a \geq 0$ and $\sum_{a\in\mathcal{A}} u_a = 1$, with probability density

$$q_{\text{Dir}}(u_1,\ldots,u_C) = (C-1)!. \tag{2.21}$$

A practical procedure, for generating Dirichlet distributed samples u_a, involves transforming independent uniform samples. Specifically, we draw $C-1$ independent points y_a for $a \in \mathcal{A}_C$ from the uniform distribution $\mathcal{U}[0,1]$, sort them in ascending order and set $y_C = 1$, so that

$$0 \leq y_1 \leq y_2 \leq \cdots \leq y_{C-1} \leq y_C \equiv 1.$$

Finally, the updated volume fraction values are computed as

$$\begin{cases} u_1 = y_1 \\ u_{a+1} = y_{a+1} - y_a \quad \text{for } a = 1, \ldots, C-1 \end{cases}$$

To ensure that the average volume fraction

$$\bar{\phi}_a = \frac{1}{|\Omega|} \int_\Omega \phi_a(\boldsymbol{x})\, \boldsymbol{dx}$$

remains unchanged by the sampling procedure, the proposed configuration is rescaled as follows for $a \in \mathcal{A}_C$ as

$$\begin{cases} \phi'_a(\boldsymbol{x}_{\bar{\boldsymbol{m}}}) = u_a \\ \phi'_a(\boldsymbol{x}_{\boldsymbol{m}}) = \frac{\phi(\boldsymbol{x}_{\boldsymbol{m}})}{\alpha_a} \quad \forall \boldsymbol{m} \neq \bar{\boldsymbol{m}} \end{cases}$$

The scaling factor α_a is chosen such that

$$\bar{\phi}_a = \frac{1}{M} \sum_{\boldsymbol{m} \in \boldsymbol{M}} \phi'_a(\boldsymbol{x}_{\boldsymbol{m}}).$$

Substituting the expression for ϕ'_a in terms of ϕ_a, we obtain

$$\begin{aligned} \bar{\phi}_a = \frac{1}{M} \sum_{\boldsymbol{m} \in \boldsymbol{M}} \phi'_a(\boldsymbol{x}_{\boldsymbol{m}}) &= \frac{1}{M} \left[u_a + \sum_{\boldsymbol{m} \in \boldsymbol{M} \setminus \{\bar{\boldsymbol{m}}\}} \frac{\phi_a(\boldsymbol{x}_{\boldsymbol{m}})}{\alpha_a} \right] \\ &= \frac{1}{M} \left[u_a + \frac{1}{\alpha_a} \sum_{\boldsymbol{m} \in \boldsymbol{M}} \phi_a(\boldsymbol{x}_{\boldsymbol{m}}) - \frac{1}{\alpha_a} \phi_a(\boldsymbol{x}_{\bar{\boldsymbol{m}}}) \right] \\ &= \frac{1}{M} \left[u_a + \frac{1}{\alpha_a} M \bar{\phi}_a - \frac{1}{\alpha_a} \phi_a(\boldsymbol{x}_{\bar{\boldsymbol{m}}}) \right]. \end{aligned}$$

Then, the scaling factor α_a can be written as

$$\alpha_a = \frac{M\bar{\phi}_a - \phi_a(\boldsymbol{x}_{\bar{\boldsymbol{m}}})}{M\bar{\phi}_a - u_a}.$$

This ensures that the average volume fraction remains unchanged after the proposal step, maintaining consistency with the original system constraints.

To prove the the proposal scheme described in Algorithm 1 is reversible, we will prove that the proposal distribution is symmetric, meaning that (2.20) holds. In the scheme, a site $\bar{\boldsymbol{m}}$ is selected randomly from a set $\boldsymbol{M}$ of M discrete sites, with each site selected with equal probability

$$q_{\text{site}}(\bar{\boldsymbol{m}}) = \frac{1}{M}.$$

Since the reverse move also selects a site with uniform probability, this part of the proposal is symmetric. At a chosen site, new volume fractions u_a are sampled from a Dirichlet distribution. As can be seen in Eq. (2.21), this distribution is invariant under permutation of its inputs and thus provides a symmetric sampling rule.

However, this does not guarantee reversibility because the rescaling step modifies all other components. To prove reversibility, we can check that if the transformation $\phi_a \to \phi'_a$ rescales all $\phi_a(\boldsymbol{x_m})$ except for $\phi_a(\boldsymbol{x_{\bar{m}}})$, then the reverse transformation $\phi'_a \to \phi_a$ rescales using $\alpha'_a = 1/\alpha_a$, meaning that the original field ϕ_a can be reconstructed by applying the same rule in reverse. Indeed, in the reverse transformation $\phi'_a \to \phi''_a$, the probability to select the same site $\boldsymbol{\bar{m}}$ and the probability to sample new volume fraction values $u'_a = \phi_a(\boldsymbol{x_m})$ equal to the ones of the original fields in $\boldsymbol{x_m}$ are the same to the probabilities in the direct transformation. On the other hand, given the site $\boldsymbol{\bar{m}}$ and the values u'_a the rescaling is a deterministic procedure, that impose

$$\bar{\phi}_a = \frac{1}{M} \sum_{\boldsymbol{m} \in \boldsymbol{M}} \phi''_a(\boldsymbol{x_m}),$$

where we have

$$\begin{cases} \phi''_a(\boldsymbol{x_{\bar{m}}}) = u'_a = \phi_a(\boldsymbol{x_{\bar{m}}}) \\ \phi''_a(\boldsymbol{x_m}) = \frac{\phi'_a(\boldsymbol{x_m})}{\alpha'_a} = \frac{\phi_a(\boldsymbol{x_m})}{\alpha_a \alpha'_a} \quad \forall \boldsymbol{m} \neq \boldsymbol{\bar{m}} \end{cases}$$

Therefore, we have

$$\begin{aligned} \bar{\phi}_a = \frac{1}{M} \sum_{\boldsymbol{m} \in \boldsymbol{M}} \phi''_a(\boldsymbol{x_m}) &= \frac{1}{M} \left[\phi_a(\boldsymbol{x_m}) + \sum_{\boldsymbol{m} \in \boldsymbol{M} \setminus \{\boldsymbol{m}\}} \frac{\phi_a(\boldsymbol{x_m})}{\alpha_a \alpha'_a} \right] \\ &= \frac{1}{M} \left[\phi_a(\boldsymbol{x_m}) + \frac{1}{\alpha_a \alpha'_a} \sum_{\boldsymbol{m} \in \boldsymbol{M}} \phi_a(\boldsymbol{x_m}) - \frac{1}{\alpha_a \alpha'_a} \phi_a(\boldsymbol{x_{\bar{m}}}) \right] \\ &= \frac{1}{M} \left[\phi_a(\boldsymbol{x_m}) + \frac{1}{\alpha_a \alpha'_a} M \bar{\phi}_a - \frac{1}{\alpha_a \alpha'_a} \phi_a(\boldsymbol{x_{\bar{m}}}) \right]. \end{aligned}$$

Then, it is immediate to see that the scaling factor of the reverse transformation α'_a satisfies

$$\alpha'_a = \frac{1}{\alpha_a}.$$

Therefore, the transformation $\phi_a \to \phi'_a$ is invertible, as with a proper choice of the perturbed site $\boldsymbol{\bar{m}}$ and of the new volume fractions, the transformation $\phi'_a \to \phi''_a$ completely recovers the original fields, meaning that $\phi''_a = \phi_a$.

This proves that the proposal is symmetric and reversible. Since reversibility ensures that detailed balance holds, the Metropolis-Hastings Algorithm 2 correctly samples from the equilibrium distribution.

2.6.2 Equilibrium sampling results

To evaluate the effect of thermal fluctuations on an equilibrium phase-separated system, we applied the Metropolis-Hastings algorithm to generate equilibrium configurations. While the Metropolis-Hastings method, in principle, allows direct sampling from

Algorithm 2 Metropolis-Hastings

```
Require: $\boldsymbol{\phi}^{(0)}$ initial state
Require: $\boldsymbol{\theta}$ vector of parameters
Require: $\beta$ inverse thermal energy
Require: $N_{\text{MC}}$ number of Monte Carlo steps
  for $i = 1$ to $N_{\text{MC}}$ do
      Propose a new configuration $\boldsymbol{\phi}'$ using Algorithm 1
      Compute the free energy difference $\Delta F = F(\boldsymbol{\phi}'|\boldsymbol{\theta}) - F(\boldsymbol{\phi}^{(i)}|\boldsymbol{\theta})$
      Compute the acceptance probability
          $p_{\text{accept}} = \min\left\{1,\ e^{-\beta \Delta F}\right\}$
      Sample a uniform random number $r \sim \mathcal{U}[0,1]$
      if $r < p_{\text{accept}}$ then
          Accept the move: $\boldsymbol{\phi}^{(i+1)} \leftarrow \boldsymbol{\phi}'$
      else
          Reject the move: $\boldsymbol{\phi}^{(i+1)} \leftarrow \boldsymbol{\phi}^{(i)}$
      end if
  end for
  Return equilibrium configuration $\boldsymbol{\phi}^{(N_{\text{MC}})}$
```

the Boltzmann distribution, achieving full convergence starting from a homogeneous or random initial condition requires an impractically long simulation time. To go around this limitation, we first evolved the system using the Cahn-Hilliard model until it reached a near-equilibrium state as described in Section 2.5.1. The Metropolis-Hastings algorithm was then applied to introduce fluctuations while preserving the equilibrium structure. This approach allows us to explore the effects of introducing microscopic noise to an already equilibrated system, mimicking the presence of thermal fluctuations in a real environment.

The sampling was performed only for the binary mixture case and we initialized the Metropolis-Hastings algorithm using the final configuration obtained from the Cahn-Hilliard simulation represented in Figure 2.1c, where the system had already reached a well-defined phase-separated state. By varying the interaction parameter χ and the gradient coefficient κ, we explored how fluctuations influence the equilibrium configuration.

For interaction parameters $\chi = 500$ and $\kappa = 50$, the introduction of thermal fluctuations significantly disrupted the equilibrium structure. Despite these values being much larger than those used in the Cahn-Hilliard simulation, the equilibrium pattern was not preserved, menaing that even minimal levels of fluctuations were sufficient to disrupt the established equilibrium structure. This suggests that at these parameter values, the system is not sufficiently stabilized by thermodynamic forces, allowing fluctuations to drive it toward a more mixed state. Figure 2.4 shows the last state of the Metropolis sampling process, along with the evolution of the free energy over the course of the simulation.

Increasing the interaction parameters to $\chi = 1000$ and $\kappa = 100$, we observed that the overall phase-separated pattern was preserved, but noise was introduced throughout the interface regions. The fluctuations perturb the boundaries between phases but do not fully dissolve the existing domains, as showed in Figure 2.5. This suggests that stronger interactions provide greater resistance to perturbations, allowing the system to retain its phase-separated organization despite thermal fluctuations.

For even higher interaction strengths, the phase-separated structure remains robust, and fluctuations primarily sharpen the boundaries between the coexisting phases. This behavior suggests that at sufficiently strong interactions, the system exhibits a high resistance to thermal perturbations, reinforcing the sharp interfaces characteristic of phase separation.

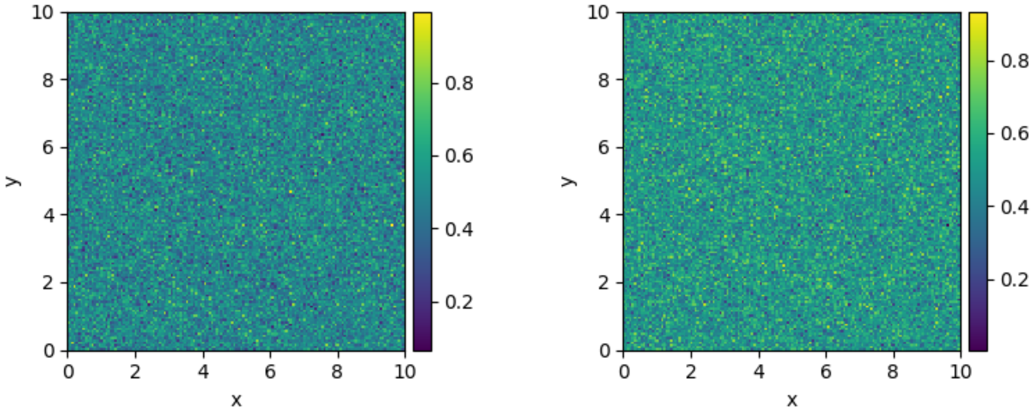

(a) Initial state at time $t = 0$.

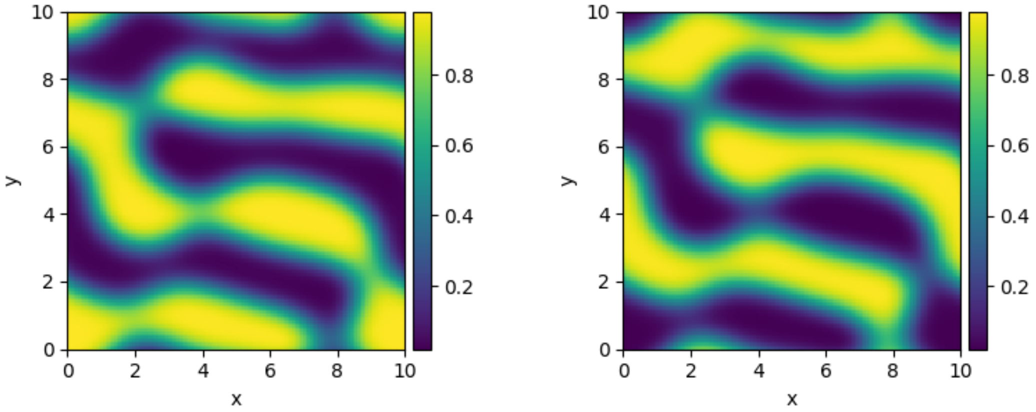

(b) State at time $t = 10^5$.

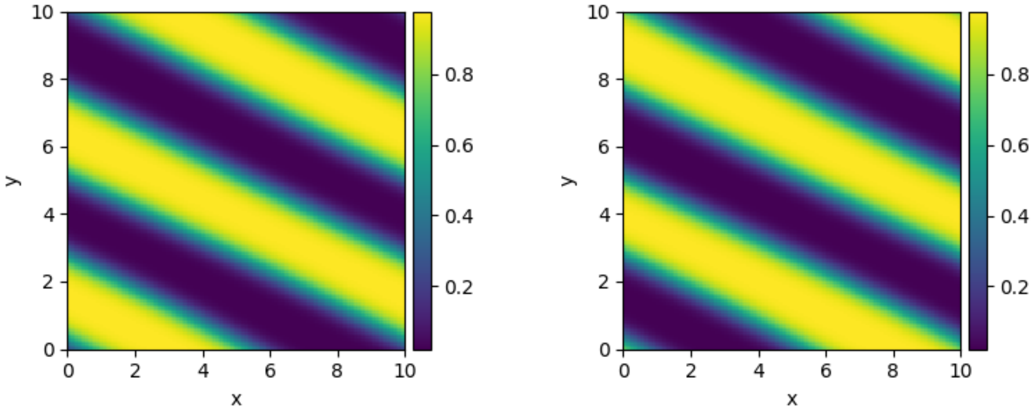

(c) Final state at time $t = 10^6$.

Figure 2.1: Numerical solution of the Cahn-Hilliard equation for volume fractions of a binary mixture on a two-dimensional domain.

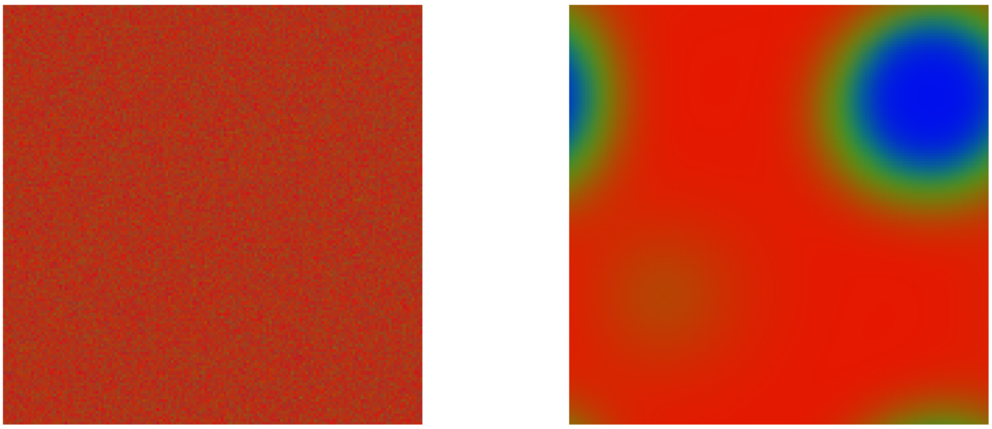

(a) Initial state at time $t = 0$

(b) Final state at time $t = 10^7$

Figure 2.2: Numerical solutions of Cahn-Hilliard equations for volume fractions of a ternary mixture on a two-dimensional domain.

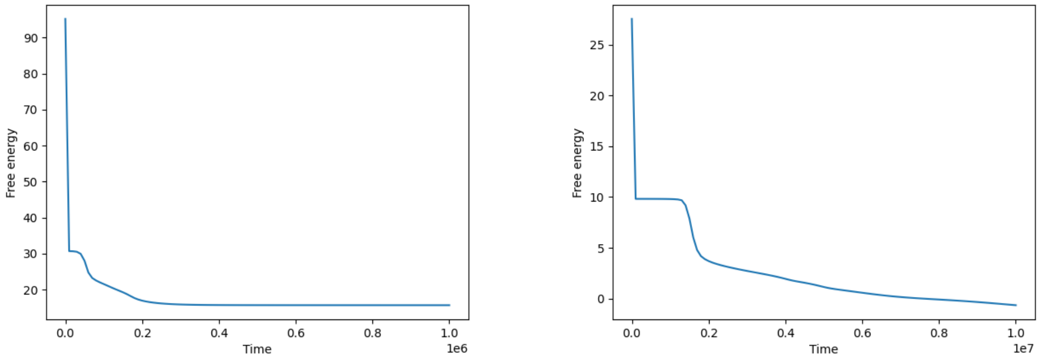

(a) Binary mixture.

(b) Ternary mixture.

Figure 2.3: Evolution of free energy over time for the binary (Figure 2.1) and ternary (Figure 2.2) mixtures simulated using the Cahn-Hilliard dynamics, as described in Section 2.5.1.

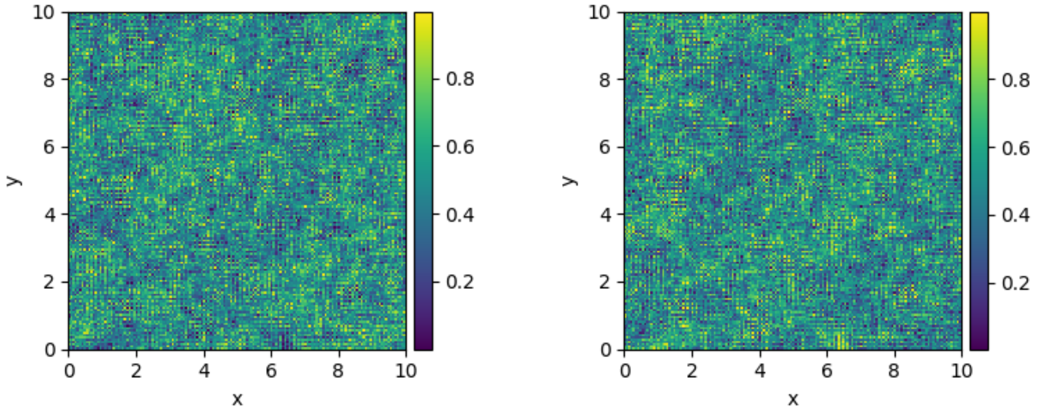

(a) Final equilibrium state obtained using the Metropolis-Hastings algorithm, showing disruption of the initial phase-separated pattern.

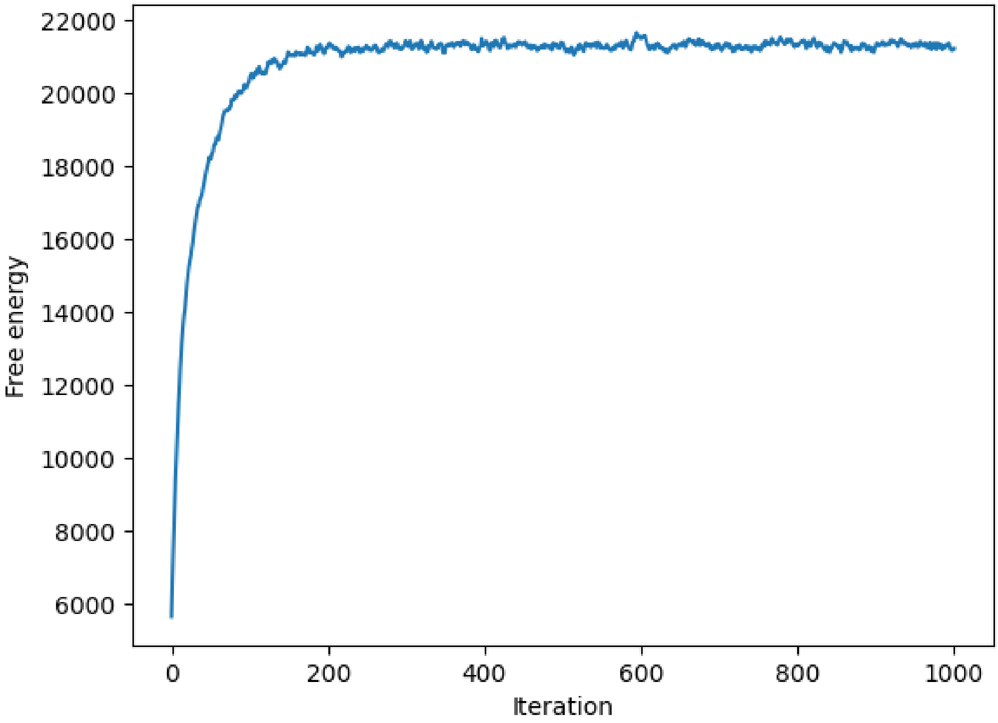

(b) Evolution of the free energy over the course of the simulation, illustrating the destabilization of the equilibrium configuration.

Figure 2.4: Effect of thermal fluctuations on phase separation stability for $\chi = 500$ and $\kappa = 50$.

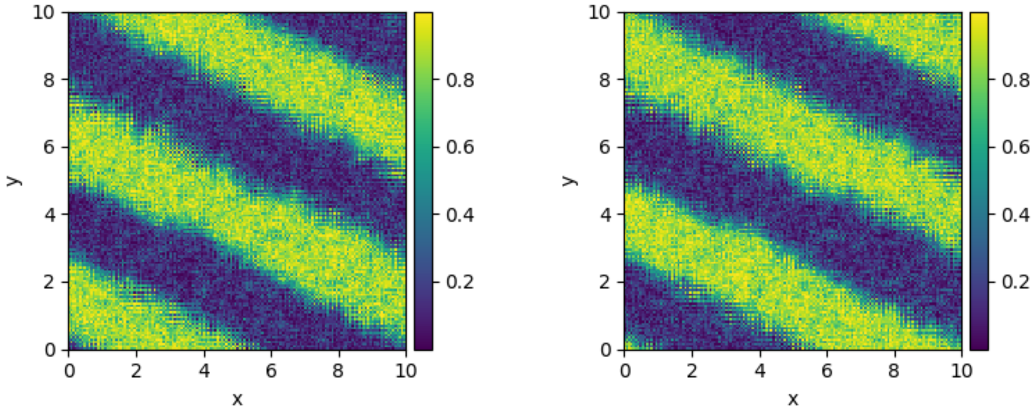

(a) Final equilibrium state obtained using the Metropolis-Hastings algorithm, showing that phase-separated pattern is largely preserved, but thermal fluctuations introduce noise within the domains.

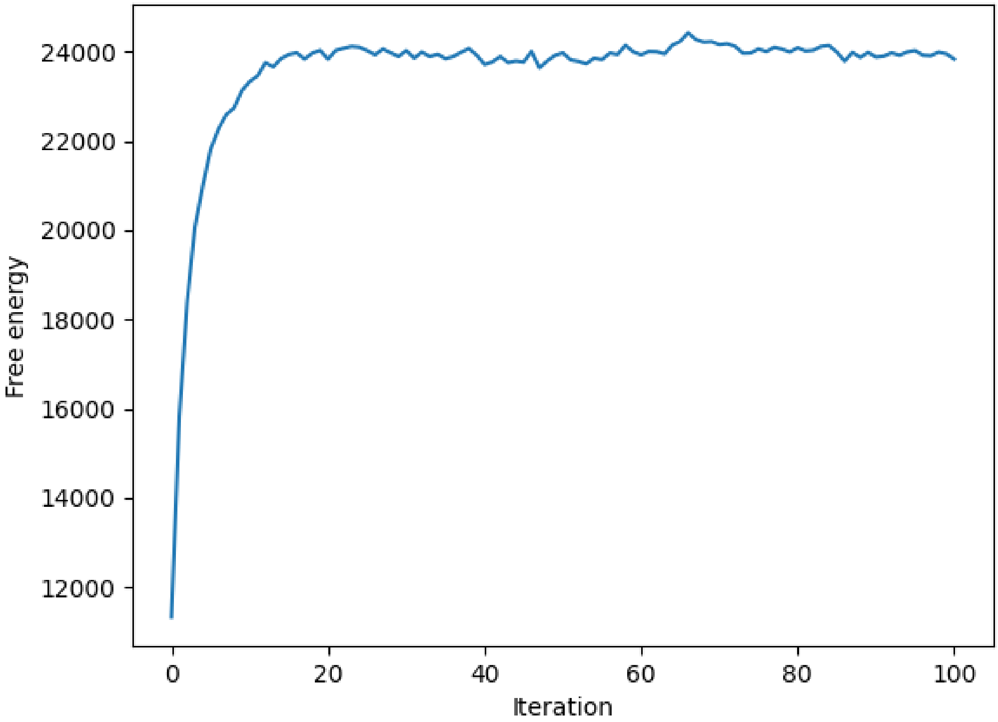

(b) Evolution of the free energy over the course of the simulation.

Figure 2.5: Effect of thermal fluctuations on phase separation stability for $\chi = 1000$ and $\kappa = 100$.

Chapter 3

Estimation of parameters for equilibrium systems

The assumption of equilibrium is a convenient starting point of modeling, because it allows characterizing static snapshot data. Reaching equilibrium, phase-separating systems present coexisting droplets of different components. Their spatial organization reflects the underlying thermodynamic parameters. A fundamental question arises: can we infer the parameters governing equilibrium configurations from a single snapshot? If so, this would provide a powerful approach for understanding phase separation without requiring full dynamical tracking.

In this Chapter, we explore how to estimate equilibrium parameters using both the least squares method and Bayesian inference, two widely used approaches for fitting models to data. The least squares method provides a deterministic estimation technique by solving an overdetermined system of equations that arise from the equilibrium conditions. Bayesian inference, on the other hand, offers a probabilistic framework that can be useful in dealing with noise in experimental data and exploring parameter distributions.

We will discuss a range of possible implementations tailored for different estimation purposes and illustrate its effectiveness through case studies. Exploiting the procedures for generating equilibrium states established in Sections 2.5 and 2.6, we generate reference configurations and design tests for validating the estimation techniques. These equilibrium states provide a controlled environment, where the accuracy and robustness of the estimation methods can be assessed.

3.1 Least squares method

The least squares estimation procedure relies on the fundamental assumption that at equilibrium, the system satisfies the stationarity condition of the dynamic equations. Specifically, under equilibrium conditions, the net fluxes of all components must vanish.

Given the continuity equation (2.7), the equilibrium condition simplifies to the requirement that the flux must be identically zero for each $a \in \mathcal{A}_C$, so that

$$\boldsymbol{j}_a = \mathbf{0}.$$

By definition of the flux (2.8) and assuming that the mobility function Λ_a is strictly positive, the equilibrium condition reduces to

$$\nabla \mu_a = \nabla \left(\frac{\delta F}{\delta \phi_a} \right) = \mathbf{0}.$$

Expanding this expression using the functional derivative of the free energy, we obtain the equilibrium condition

$$\partial_r \left[\frac{\log \phi_a}{N_a} - \frac{\log \left(1 - \sum_{b \in \mathcal{A}_C} \phi_b\right)}{N_C} + \sum_{b \in \mathcal{A}_C} \left(\chi_{ab} - \chi_{bC} - \chi_{aC} \right) \phi_b - \sum_{b \in \mathcal{A}_C} \kappa_{ab} \nabla^2 \phi_b \right] = 0, \tag{3.1}$$

for $a \in \mathcal{A}_C$ and $r = 1, \ldots, d$.

It is important to note that this equilibrium condition only requires $\Lambda_a > 0$, meaning that the specific choice of diffusion coefficient does not impact the final equilibrium configuration. Consequently, in numerical simulations where the primary interest lies in the final equilibrium state, Λ can be treated as a computational parameter rather than a physically constrained quantity. This flexibility allows us to define Λ in the most convenient way as a function of volume fractions, to optimize computational efficiency while preserving the system's fundamental behavior.

3.1.1 Formulating the least squares problem

The equilibrium condition can be expressed in terms of the spectral modes. Consider the basis functions of the spectral approximation defined according to (2.13), then we can project the Eq. (3.1) onto the approximation subspace, obtaining for $a \in \mathcal{A}_C$, $\boldsymbol{j} \in J$ and $r = 1, \ldots, d$

$$\langle \partial_r \mu_a, e_{\boldsymbol{j}} \rangle = 0.$$

The application of pseudo-spectral methods leads to a linear system in terms of the unknown thermodynamic parameters χ_{ab}, κ_{ab} and N_a. This system is typically overdetermined, meaning that there are more equations than unknowns. The least squares method provides a way to minimize the residual error and extract an estimation of the parameters that describe the equilibrium configuration. Thus, given an equilibrium state $\{\phi_a\}_{a \in \mathcal{A}_C}$, we compute the Fourier modes $\{\widehat{\phi}_a = \mathfrak{F}\phi_a\}_{a \in \mathcal{A}_C}$ and recast the equilibrium condition as a linear least squares problem

$$\arg\min_{\boldsymbol{\theta}} \left\| \boldsymbol{b} - A\boldsymbol{\theta} \right\|,$$

where A encodes the equilibrium condition, $\boldsymbol{\theta}$ represents the unknown interaction parameters and $\boldsymbol{b}$ is the known term of the linear system.

To introduce some explicit forms of the linear system, depending on the available information, let us notice that we can write the partial derivative of the basis function $e_{\boldsymbol{j}}$ as

$$\partial_r e_{\boldsymbol{j}} = \partial_r e_{j_1,\dots,j_d} = -\frac{2\pi j_r}{L_r} e_{j_1,\dots,-j_r,\dots,j_d}. \tag{3.2}$$

Then, we project term by term the equation (3.1) onto the spectral approximation space. Last two terms give

$$\begin{aligned}
\langle \partial_r \phi_a, e_{\boldsymbol{j}} \rangle &= \sum_{\boldsymbol{k}\in J} \widehat{\phi}_{a,\boldsymbol{k}} \langle \partial_r e_{\boldsymbol{k}}, e_{\boldsymbol{j}} \rangle = \sum_{\boldsymbol{k}\in J} \widehat{\phi}_{a,\boldsymbol{k}} \frac{2\pi}{L_r}(-k_r)\langle e_{k_1,\dots,-k_r,\dots,k_d}, e_{\boldsymbol{j}} \rangle \\
&= \sum_{\boldsymbol{k}\in J} \widehat{\phi}_{a,\boldsymbol{k}} \frac{2\pi}{L_r}(-k_r)\delta_{(k_1,\dots,-k_r,\dots,k_d),\boldsymbol{j}} \\
&= \sum_{\boldsymbol{k}\in J} \widehat{\phi}_{a,\boldsymbol{k}} \frac{2\pi}{L_r}(-k_r)\delta_{k_1,j_1}\cdots\delta_{-k_r,j_r}\delta_{k_d,j_d} \\
&= \widehat{\phi}_{a,(j_1,\dots,-j_r,\dots,j_d)} \frac{2\pi j_r}{L_r}, \\
\langle \partial_r \nabla^2 \phi_a, e_{\boldsymbol{j}} \rangle &= \sum_{\boldsymbol{k}\in J} g_{\boldsymbol{k}} \widehat{\phi}_{a,\boldsymbol{k}} \langle \partial_r e_{\boldsymbol{k}}, e_{\boldsymbol{j}} \rangle = \sum_{\boldsymbol{k}\in J} g_{\boldsymbol{k}} \widehat{\phi}_{a,\boldsymbol{k}} \frac{2\pi}{L_r}(-k_r)\langle e_{k_1,\dots,-k_r,\dots,k_d}, e_{\boldsymbol{j}} \rangle \\
&= \sum_{\boldsymbol{k}\in J} g_{\boldsymbol{k}} \widehat{\phi}_{a,\boldsymbol{k}} \frac{2\pi}{L_r}(-k_r)\delta_{(k_1,\dots,-k_r,\dots,k_d),\boldsymbol{j}} \\
&= g_{j_1,\dots,-j_r,\dots,j_d} \widehat{\phi}_{a,(j_1,\dots,-j_r,\dots,j_d)} \frac{2\pi j_r}{L_r}.
\end{aligned}$$

On the other hand, for the logarithmic term integrating by parts and applying periodic boundary conditions, we get

$$\begin{aligned}
\langle \partial_r \log \phi_a, e_{\boldsymbol{j}} \rangle &= \int_\Omega \partial_r \left[\log\left(\phi_a(\boldsymbol{x})\right)\right] e_{\boldsymbol{j}}(\boldsymbol{x})\, \boldsymbol{dx} \\
&= \int_0^{L_d} \cdots \int_0^{L_1} \partial_r \left[\log\left(\phi_a(\boldsymbol{x})\right)\right] e^{\boldsymbol{j}}(\boldsymbol{x})\, dx_1 \cdots dx_d \\
&= \int_0^{L_d} \cdots \int_0^{L_{r+1}} \int_0^{L_{r-1}} \cdots \int_0^{L_1} \left\{ \log\left(\phi_a(\boldsymbol{x})\right) e_{\boldsymbol{j}}(\boldsymbol{x}) \Big|_0^{L_r} \right. \\
&\qquad \left. - \int_0^{L_r} \log\left(\phi_a(\boldsymbol{x})\right) \partial_r e_{\boldsymbol{j}}(\boldsymbol{x})\, dx_r \right\} dx_1 \cdots dx_{r-1}\, dx_{r+1} \cdots dx_d \\
&= -\int_\Omega \log\left(\phi_a(\boldsymbol{x})\right) \partial_r e_{\boldsymbol{j}}(\boldsymbol{x})\, \boldsymbol{dx} \\
&= -\langle \log \phi_a, \partial_r e_{\boldsymbol{j}} \rangle = -\frac{2\pi}{L_r}(-j_r)\langle \log \phi^a, e_{j_1,\dots,-j_r,\dots,j_d} \rangle \\
&= \frac{2\pi j_r}{L_r} \langle \log \phi_a, e_{j_1,\dots,-j_r,\dots,j_d} \rangle.
\end{aligned}$$

Therefore, the equilibrium condition translates to

$$\begin{aligned} &\frac{2\pi j_r}{L_r}\left\langle \frac{\log\left(\mathfrak{F}^*\widehat{\phi}_a\right)}{N_a}, e_{j_1,\dots,-j_r,\dots,j_d}\right\rangle - \frac{2\pi j_r}{L_r}\left\langle \frac{\log\left(1-\sum_{b\in\mathcal{A}_C}\mathfrak{F}^*\widehat{\phi}_b\right)}{N_C}, e_{j_1,\dots,-j_r,\dots,j_d}\right\rangle \\ &\qquad + \sum_{b\in\mathcal{A}_C}\left(\chi_{ab}-\chi_{bC}-\chi_{aC}\right)\frac{2\pi j_r}{L_r}\widehat{\phi}_{b,(j_1,\dots,-j_r,\dots,j_d)} \\ &\qquad - \sum_{b\in\mathcal{A}_C}\kappa_{ab}\frac{2\pi j_r}{L_r}g_{j_1,\dots,-j_r,\dots,j_d}\widehat{\phi}_{b,(j_1,\dots,-j_r,\dots,j_d)} = 0, \end{aligned} \tag{3.3}$$

for each $a\in\mathcal{A}_C$, $r=1\dots,d$ and $\boldsymbol{j}\in J$.

In the framework of Flory-Huggins solution theory, by definition of N_a is a relative size of the molecules of component a normalized with respect to the size of component C, therefore N_C is known and unitary. Given an equilibrium state $\{\phi_a\}_{a\in\mathcal{A}_C}$, the modes $\{\widehat{\phi}_a\}_{a\in\mathcal{A}_C}$ can be computed. Looking at the set of equations (3.3) as an overdetermined linear system, where the variables are the $(C-1)(C+1)$ parameters of the Cahn-Hilliard model, i.e. $C-1$ molecular sizes N_a for $a\in\mathcal{A}_C$, $C(C-1)/2$ interaction parameters $\chi_{ab}=\chi_{ba}$ for $a\neq b$, $a,b\in\mathcal{A}_C$ and $C(C-1)/2$ gradient coefficients κ_{ab} for $a,b\in\mathcal{A}_C$. This interpretation allows us to apply linear least squares method to infer the set of parameters that generated such equilibrium state.

First, let us suppose that the only information on the system that we have are the equilibrium state ϕ_a for $a\in\mathcal{A}_C$ and an estimate of the size v_C of the particles of component C. Then, we can define the known term for $a\in\mathcal{A}_C$ and $\boldsymbol{j}\in J$

$$b^{(1)}_{a,\boldsymbol{j}} := -\frac{2\pi j_r}{L_r}\left\langle \frac{\log\left(1-\sum_{b\in\mathcal{A}_C}\mathfrak{F}^*\widehat{\phi}_b\right)}{N_C}, e_{j_1,\dots,-j_r,\dots,j_d}\right\rangle.$$

Moreover, we define the vector of variables $\boldsymbol{\theta}^{(1)}$ such that $\theta^{(1)}_k$ for $k=1,\dots,(C-1)(C+1)$ corresponds to one of the $(C-1)(C+1)$ variables N_a, χ_{ab}, κ_{ab} of the linear system, according to some ordering map. Once the order on the variables has been established, it is possible to introduce a tensor $A^{(1)}_{a,\boldsymbol{j},k}$ for $a\in\mathcal{A}_C$, $\boldsymbol{j}\in J$ and $k\in\{1,\dots,(C-1)(C+1)\}$ such that the equilibrium condition can be written component-wise as

$$\sum_{k=1}^{(C-1)(C+1)} A^{(1)}_{a,\boldsymbol{j},k}\theta^{(1)}_k = b^{(1)}_{a,\boldsymbol{j}}.$$

Finally, an estimation of the parameters $\theta^{(1)}_k$ can be found solving the problem in the least squares sense. Namely, we solve the following problem

$$\underset{\boldsymbol{\theta}^{(1)}}{\arg\min}\left\|\boldsymbol{b}^{(1)}-A^{(1)}\boldsymbol{\theta}^{(1)}\right\|_2.$$

However, the presence of noise in the equilibrium state can impact the accuracy of this inference technique. Additionally, in some cases, supplementary information about the system may be available. For instance, we might have access to the relative sizes N_a

from existing literature. In such scenarios, incorporating this additional data alongside the information on N_C can improve the accuracy of parameter estimation, leading to more reliable predictions. In this case the definition of the known term would be

$$b^{(2)}_{a,\boldsymbol{j}} := \frac{2\pi j_r}{L_r}\left\langle \frac{\log\left(\mathfrak{F}^*\widehat{\phi}_a\right)}{N_a}, e_{j_1,\dots,-j_r,\dots,j_d}\right\rangle - \frac{2\pi j_r}{L_r}\left\langle \frac{\log\left(1-\sum_{b\in\mathcal{A}_C}\mathfrak{F}^*\widehat{\phi}_b\right)}{N_C}, e_{j_1,\dots,-j_r,\dots,j_d}\right\rangle .$$

Then, we can accordingly define the vector $\boldsymbol{\theta}^{(2)}$ of $C(C-1)$ components containing the parameters χ_{ab} and κ_{ab} and the corresponding tensor $A^{(2)}$ such that $A^{(2)}_{a,\boldsymbol{j},k}\theta^{(2)}_k = b^{(2)}_{a\,\boldsymbol{j}}$. Finally, we proceed as before solving the problem in the leas squares sense to get an estimation of parameters $\boldsymbol{\theta}^{(2)}$.

Another common scenario involves the assumption that there exists some linear relation between κ_{ab} and χ_{cd}. For instance, we can express each κ_{ab} in terms of χ_{cd} referring to [20, 21, 25] as

$$\kappa_{ab} = \frac{1}{6}\left[(R_a^2+R_C^2)\chi_{aC} + (R_b^2+R_C^2)\chi_{bC} - (R_a^2+R_a^2)\chi_{ab}\right], \tag{3.4}$$

for $a, b \in \mathcal{A}_C$, where R_a are the radii of gyration for each component.

By selecting a specific form for the known term $\boldsymbol{b}^{(i)}$ and substituting the expressions for κ_{ab} into the equilibrium condition, we can now define the vector of variables $\bar{\boldsymbol{\theta}}^{(i)}$. The dimension of $\bar{\boldsymbol{\theta}}^{(i)}$ depends on whether the relative sizes N_a are included as variables. If we use $\boldsymbol{b}^{(1)}$, the sizes N_a are considered as variables and $\bar{\boldsymbol{\theta}}^{(1)}$ has $\frac{(C-1)(C+2)}{2}$. If we use $\boldsymbol{b}^{(1)}$, then N_a are supposed to be known and $\bar{\boldsymbol{\theta}}^{(2)}$ has $\frac{C(C-1)}{2}$ components. Consequently, we can introduce the tensor $\bar{A}^{(i)}$ such that $\bar{A}\bar{\boldsymbol{\theta}}^{(i)} = \boldsymbol{b}^{(i)}$ and get and estimate of $\bar{\boldsymbol{\theta}}^{(i)}$ solving the corresponding problem in least squares sense.

3.1.2 Consistency of the estimations

To validate the robustness and reliability of the parameter estimation framework, we test its consistency by applying it to equilibrium states generated from known parameter values. The objective is to verify whether the inferred parameters $\widetilde{\theta}_k$ closely match the expected ones $\widetilde{\theta}_k$ within a small relative error. This step ensures that the least squares approach effectively recovers the thermodynamic parameters governing phase separation. The accuracy of the estimation is assessed by comparing the inferred parameter values $\widetilde{\theta}_k$ with the expected ones θ_k and is quantified through the relative error, which is computed for each parameter as

$$\left|\frac{\theta_k - \widetilde{\theta}_k}{\theta_k}\right| .$$

A low relative error indicates that the estimation framework accurately retrieves the underlying model parameters from the equilibrium state.

Additionally, we assess the uncertainty of the inferred parameters by computing their standard errors. The standard error for each parameter $\widetilde{\theta}_k$ is obtained from the covariance matrix of the least squares estimates, as

$$\mathrm{SE}(\widetilde{\theta}_k) = \sqrt{\mathrm{Cov}(\widetilde{\boldsymbol{\theta}})_{kk}},$$

where the covariance matrix is given by $\mathrm{Cov}(\widetilde{\boldsymbol{\theta}}) = \widetilde{\sigma}^2(A^\top A)^{-1}$ and the residual variance $\hat{\sigma}^2$ is estimated as

$$\widetilde{\sigma}^2 = \frac{1}{n-K}\sum_{i=1}^{n} r_i$$

where K is the number of estimated parameters, n is the number of observations given by $n = (C-1)Md$ and $r_i = b_i - (A\boldsymbol{\theta})_i$ are the residuals. The standard errors provide a measure of the uncertainty in each parameter estimate and a low value of $\mathrm{SE}(\widetilde{\theta}_k)$ confirms the reliability of the inferred parameters. In the following, report the relative standard error, computed as $\mathrm{SE}(\widetilde{\theta}_k)/\widetilde{\theta}_k$.

Validation for a binary mixture We first consider the binary mixture represented in Figure 2.1, whose equilibrium state is known to be generated by specific values of χ, κ and N_1. The least squares method is applied on the equilibrium state to infer these parameters and the results are summarized in Table 3.1. The inferred values show agreement with the expected values, within a relative errors of 1%, corroborating the effectiveness of the method.

Parameter	Expected	Inferred	Relative Error (%)	Standard Error (%)
χ	4	3.9955	0.11	0.016
κ	0.5	0.4966	0.69	0.023
N_1	1	1.0001	0.02	0.026

Table 3.1: Comparison between expected and inferred parameter values for a binary mixture, using the least squares method.

Next, we assume that additional prior information about the system is available. Specifically we assume that the molecular size ratio N_1 is known and apply the least squares method to infer only χ and κ. The results, presented in Table 3.2, indicate a further reduction in relative errors, confirming that incorporating prior knowledge enhances the accuracy of the parameter estimation.

Parameter	Expected	Inferred	Relative Error (%)	Standard Error (%)
χ	4	3.9959	0.10	0.009
κ	0.5	0.4966	0.68	0.018

Table 3.2: Comparison between expected and inferred parameter values for a binary mixture, when the molecular size ratio N_1 is known, using the least squares method.

Similarly, we examine cases where κ or both κ and N_1. are known, allowing us to infer only the remaining parameters. The results, displayed in Tables 3.3 and 3.4, show a consistent reduction in relative errors, reinforcing the idea that incorporating additional constraints improves the reliability of the inference.

Parameter	Expected	Inferred	Relative Error (%)	Standard Error (%)
χ	4	3.9971	0.07	0.018
N_1	1	1.0002	0.02	0.030

Table 3.3: Comparison between expected and inferred parameter values, when κ is known, using the least squares method.

Parameter	Expected	Inferred	Relative Error (%)	Standard Error (%)
χ	4	3.998	0.06	0.010

Table 3.4: Comparison between expected and inferred parameter values, when both κ and N_1 are known, using the least squares method.

Validation for a ternary mixture To further validate the robustness of the approach, we extend the analysis to a ternary mixture, illustrated in Figure 2.2. In this case, multiple interaction parameters χ_{ab}, gradient parameters κ_{ab} and molecular size ratios N_a need to be inferred. Table 3.5 show that most inferred values closely match the expected ones, though slightly higher relative errors are observed for χ_{12}, χ_{23} and N_2, suggesting that additional constraints could further improve accuracy.

When prior knowledge of the molecular size ratios N_1 and N_2 is available, the estimation accuracy improves significantly, as shown in Table 3.6.

Next, we refine the estimations assuming that the gradient parameters κ_{ab} are known and we infer only the interaction parameters χ_{ab} and the molecular size ratios N_a. The results, shown in Table 3.7, demonstrate a noticeable improvement in accuracy compared to the unconstrained case. The relative errors for χ_{12} and χ_{23}, which were previously higher, have been significantly reduced. Moreover, the inferred values for N_1 and N_2 are now closer to their expected values, indicating that fixing κ_{ab} improves parameter estimation.

Finally, we test the estimation accuracy when both the gradient parameters κ_{ab} and the molecular size ratios N_1 and N_2 are known. This represents the most constrained scenario, where only the interaction parameters χ_{ab} are inferred. The results, presented in Table 3.8, show further reductions in relative errors, with all parameters inferred with high precision.

These results confirm the reliability and consistency of the least squares estimation framework, demonstrating improved accuracy when prior information is incorporated. In cases where all parameters are inferred, small deviations can arise, particularly in complex multicomponent systems. However, incorporating additional constraints, such as known gradient energy parameters or molecular size ratios, significantly improves the accuracy of the inferred values, reinforcing the robustness of the method.

Parameter	Expected	Inferred	Relative Error (%)	Standard Error (%)
χ_{12}	3	2.683	10.6	1.127
χ_{13}	6	5.960	0.7	0.112
χ_{23}	3	2.735	8.8	1.114
κ_{11}	0.5	0.487	2.6	0.344
κ_{12}	0.1	0.103	3.4	1.104
κ_{22}	0.5	0.464	7.1	0.841
N_1	1	1.007	0.7	0.214
N_2	1	1.107	10.7	1.08

Table 3.5: Comparison between expected and inferred parameter values for a ternary mixture, using the least squares method.

Parameter	Expected	Inferred	Relative Error (%)	Standard Error (%)
χ_{12}	3	2.924	2.5	0.094
χ_{13}	6	5.980	0.3	0.021
χ_{23}	3	2.979	0.7	0.072
κ_{11}	0.5	0.490	2.0	0.099
κ_{12}	0.1	0.102	2.5	0.351
κ_{22}	0.5	0.493	1.4	0.123

Table 3.6: Comparison between expected and inferred parameter values for a ternary mixture, when molecular size ratios N_1 and N_2 are known, using the least squares method.

3.2 Bayesian inference

Bayesian inference provides a probabilistic framework for estimating the parameters of a model given observed data. Unlike standard least squares estimation, which finds a single set of parameters that minimizes the residual error, Bayesian inference explicitly treats the parameters as random variables and constructs a posterior probability distribution over possible parameter values, offering direct quantification of uncertainty.

In this framework, parameters $\boldsymbol{\theta}$ are treated as random variables with an associated probability distribution, rather than fixed values to be optimized. The central idea of Bayesian inference is to update our beliefs about the parameters given observed configuration $\boldsymbol{\phi}$, using Bayes' theorem, which states

$$p(\boldsymbol{\theta}|\boldsymbol{\phi}) = \frac{p(\boldsymbol{\phi}|\boldsymbol{\theta})p(\boldsymbol{\theta})}{p(\boldsymbol{\phi})}. \tag{3.5}$$

Here, the posterior distribution $p(\boldsymbol{\theta}|\boldsymbol{\phi})$ represents the updated belief about the parameters

Parameter	Expected	Inferred	Relative Error (%)	Standard Error (%)
χ_{12}	3	2.907	3.0	0.201
χ_{13}	6	5.978	0.4	0.039
χ_{23}	3	2.947	1.8	0.198
N_1	1	0.995	0.5	0.075
N_2	1	0.987	1.3	0.203

Table 3.7: Comparison between expected and inferred parameter values for a ternary mixture, when gradient parameters κ_{ab} are known, using the least squares method.

Parameter	Expected	Inferred	Relative Error (%)	Standard Error (%)
χ_{12}	3	2.946	1.8	0.089
χ_{13}	6	5.988	0.2	0.020
χ_{23}	3	2.985	0.5	0.072

Table 3.8: Comparison between expected and inferred parameter values for a ternary mixture, when both gradient parameters κ_{ab} and molecular size ratios N_1 and N_2 are known, using the least squares method.

after observing the data; the likelihood $p(\boldsymbol{\phi}|\boldsymbol{\theta})$ models how probable the observed data $\boldsymbol{\phi}$ are, given a specific choice of parameters $\boldsymbol{\theta}$; the prior distribution $p(\boldsymbol{\theta})$ encodes any prior knowledge or assumptions about the parameters before observing the data; while the evidence $p(\boldsymbol{\phi})$ serves as a normalization factor.

An important aspect to clarify in Bayesian inference is the treatment of the configuration $\boldsymbol{\phi}$. In a general probabilistic setting, under the canonical ensemble as discussed in Section 2.6, the state $\boldsymbol{\phi}$ is a random variable follows the Boltzmann distribution (2.18), which describes the probability of observing a particular state $\boldsymbol{\phi}$ given a fixed set of thermodynamic parameters. However, in the context of parameter estimation, we assume that $\boldsymbol{\phi}$ is already observed, meaning that we treat it as a fixed dataset rather than a true random variable. Mathematically, however, Bayes' theorem still treats $\boldsymbol{\phi}$ as random because the likelihood function $p(\boldsymbol{\phi}|\boldsymbol{\theta})$ is defined over possible states.

The inference problem reduces to estimating the parameters $\boldsymbol{\theta}$ that best explain a given an observed equilibrium configuration $\boldsymbol{\phi}$. In this framework, the Bayes' theorem reduces to

$$p(\boldsymbol{\theta}|\boldsymbol{\phi}) \propto p(\boldsymbol{\phi}|\boldsymbol{\theta})p(\boldsymbol{\theta}),$$

which can be further simplified if a non-informative prior $p(\boldsymbol{\theta})$ is chosen. Indeed, if we consider a uniform distribution, the probability $p(\boldsymbol{\theta})$ can be treated as a normalization factor, leading to

$$p(\boldsymbol{\theta}|\boldsymbol{\phi}) \propto p(\boldsymbol{\phi}|\boldsymbol{\theta}).$$

3.2.1 Reformulating the free energy

Since the likelihood $p(\boldsymbol{\phi}|\boldsymbol{\theta})$ follows the Boltzmann distribution (2.18), the free energy $F(\boldsymbol{\phi}|\boldsymbol{\theta})$ plays a central role in parameter estimation. Furthermore, it is important to notice that for a fixed state $\boldsymbol{\phi}$, the free energy reduces to a linear function with respect to the vector of parameters $\boldsymbol{\theta}$.

To make this explicit, consider that in Flory-Huggins framework, the molecular size of the solvent is set to $N_C = 1$. Given a fixed configuration $\boldsymbol{\phi}$ the free energy can then be rewritten by eliminating the constant term associated with N_C. Throughout the remainder of this section, we adopt this adjusted form of the free energy, corresponding to Eq. (2.6) with the term related to N_C removed.

This simplification is justified by by two key observations. First, in thermodynamics, energy is defined up to an arbitrary additive constant, meaning that removing a constant term does not affect the physical predictions of the model.Second, within the Bayesian framework, this constant appears in the likelihood function purely as a normalization factor, which does not influence parameter estimation. Furthermore, as will become evident in the following analysis, the estimation of individual parameters remains independent. This implies that incorporating prior knowledge about specific parameters does not necessarily enhance the accuracy of the inference for the others, reinforcing the validity of treating the free energy in this adjusted form.

To express the free energy in a form that clearly shows its linearity in the parameters $\boldsymbol{\theta}$, we introduce an explicit form of parameter vector

$$\boldsymbol{\theta} = \left(\{N_a^{-1}\}_{a\in\mathcal{A}_C},\ \{\chi_{ab}\}_{\substack{a,b\in\mathcal{A},\\ a<b}},\ \{\kappa_{ab}\}_{\substack{a,b\in\mathcal{A}_C\\ a\leq b}} \right),$$

which is a vector of $K := (C-1)(C+1)$ elements, where the first $C-1$ components contain the inverse of molecular sizes N_a^{-1}, then the $C(C-1)/2$ next components represent the distinct interaction parameters χ_{ab} and the last $C(C-1)/2$ components are the distinct gradient coefficients κ_{ab} according to some ordering rule.

Using this definition, we can express the free energy as

$$F(\boldsymbol{\phi}|\boldsymbol{\theta}) = \sum_{k=1}^{K} \theta_k \Sigma_k(\boldsymbol{\phi}), \tag{3.6}$$

where $\Sigma_k(\boldsymbol{\phi})$ are functions that only depend on the state $\boldsymbol{\phi}$ but not on the parameters $\boldsymbol{\theta}$. Specifically, we have

$$\Sigma_k(\boldsymbol{\phi}) = \begin{cases} \int_\Omega \phi_a \log \phi_a & \text{for } \theta_k = N_a^{-1} \\ \int_\Omega \phi_a \phi_b & \text{for } \theta_k = \chi_{ab},\ a \neq b,\ a,b \neq C \\ \int_\Omega \phi_a \left(1 - \sum_{a\in\mathcal{A}_C} \phi_a\right) & \text{for } \theta_k = \chi_{aC},\ a \neq C \\ \frac{1}{2}\int_\Omega \nabla\phi_a \cdot \nabla\phi_a & \text{for } \theta_k = \kappa_{aa} \\ \int_\Omega \nabla\phi_a \cdot \nabla\phi_b & \text{for } \theta_k = \kappa_{ab},\ a \neq b \end{cases} \tag{3.7}$$

Since the state of the system is known at discrete points on a Cartesian grid, as described in Section 2.4, the evaluation of these integrals can be efficiently performed using numerical approximations. The logarithmic and interaction terms are computed using the midpoint rule, which provides a straightforward method for numerical integration. On the other hand, the gradient term can be integrated through different numerical schemes. A finite difference scheme can be applied, approximating derivatives using discrete grid-based differences, while a spectral collocation approach allows for a more precise evaluation by exploiting the Fourier representation of $\boldsymbol{\phi}$. In particular, the spectral approach gives

$$\begin{aligned}
\int_\Omega \nabla\phi_a \cdot \nabla\phi_b &= \sum_{r=1}^{d} \int_\Omega (\partial_r\phi_a)(\partial_r\phi_b) \\
&\simeq \sum_{r=1}^{d} \int_\Omega \left(\sum_{\boldsymbol{j}\in J} \widehat{\phi}_{a,\boldsymbol{j}} \partial_r e_{\boldsymbol{j}} \right) \left(\sum_{\boldsymbol{k}\in J} \widehat{\phi}_{b,\boldsymbol{k}} \partial_r e_{\boldsymbol{k}} \right) \\
&= \sum_{r=1}^{d} \sum_{\boldsymbol{j}\in J} \left(\frac{2\pi j_r}{L_r} \right)^2 \widehat{\phi}_{a,(j_1,\dots,-j_r,\dots,j_d)} \widehat{\phi}_{b,(j_1,\dots,-j_r,\dots,j_d)} \int_\Omega e^2_{j_1,\dots,-j_r,\dots,j_d} \\
&= \sum_{r=1}^{d} \sum_{\boldsymbol{j}\in J} \left(\frac{2\pi j_r}{L_r} \right)^2 \widehat{\phi}_{a,(j_1,\dots,-j_r,\dots,j_d)} \widehat{\phi}_{b,(j_1,\dots,-j_r,\dots,j_d)}.
\end{aligned}$$

3.2.2 Posterior distribution of parameters

The form of the free energy presented in Eq. (3.6) suggests that we can reformulate the Bayesian inference problem in terms of the summary statistics $\boldsymbol{\Sigma}(\boldsymbol{\phi}) = \{\boldsymbol{\Sigma}_k(\boldsymbol{\phi})\}_{k=1}^K$.

First, let us consider the free energy F as a functional of $\boldsymbol{\Sigma} \in \mathbb{R}^K$. In other words, we introduce the free energy

$$\widehat{F}(\boldsymbol{\Sigma}|\boldsymbol{\theta}) = \sum_{k=1}^{K} \theta_k \Sigma_k,$$

that is equivalent to the free energy of the system, as if we set $\boldsymbol{\Sigma} := \{\Sigma_k\}_{k=1}^K$ with Σ_k the function defined in (3.7), then we have $\widehat{F} \circ \boldsymbol{\Sigma} = F$. Indeed, it holds

$$F(\boldsymbol{\phi}|\boldsymbol{\theta}) = \sum_{k=1}^{K} \theta_k \Sigma_k(\boldsymbol{\phi}) = \widehat{F}(\boldsymbol{\Sigma}(\boldsymbol{\phi})|\boldsymbol{\theta}) = \left[\widehat{F} \circ \boldsymbol{\Sigma} \right] (\boldsymbol{\phi}|\boldsymbol{\theta}),$$

where $\boldsymbol{\Sigma}(\boldsymbol{\phi}) = \{\Sigma_k(\boldsymbol{\phi})\}_{k=1}^K$.

We assume the prior distribution of $\boldsymbol{\theta} \in \mathbb{R}^K$ to be a uniform on the K-dimensional hyperrectangle in the space of parameters, meaning that it can be written as the Cartesian product of intervals

$$\Theta := \operatorname{supp}(\boldsymbol{\theta}) = \prod_{k=1}^{K} [\theta_k^{\min}, \theta_k^{\max}],$$

where each interval is denoted by $\Theta_k := [\theta_k^{\min}, \theta_k^{\max}]$ and we assume these intervals to be compact, ensuring the integrability of the posterior distribution.

Furthermore, the introduction of $\boldsymbol{\Sigma}$ allows to rewrite the posterior probability with a little abuse of notation as $p(\boldsymbol{\phi}|\boldsymbol{\theta}) = p(\boldsymbol{\Sigma}(\boldsymbol{\phi})|\boldsymbol{\theta})$. This combined with the assumptions on the prior distribution of $\boldsymbol{\theta}$ let us rewrite the posterior probability as

$$p(\boldsymbol{\theta}|\boldsymbol{\Sigma}) \propto p(\boldsymbol{\Sigma}|\boldsymbol{\theta}).$$

Now, we introduce the normalization factor for the probability density $p(\boldsymbol{\theta}|\boldsymbol{\Sigma})$:

$$Z(\boldsymbol{\Sigma}) = \int_{\Theta} p(\boldsymbol{\theta}|\boldsymbol{\Sigma})\, \boldsymbol{d\theta},$$

so that we can express the probability density as

$$p(\boldsymbol{\theta}|\boldsymbol{\Sigma}) = \frac{e^{-\widehat{F}(\boldsymbol{\Sigma}|\boldsymbol{\theta})}}{Z(\boldsymbol{\Sigma})}.$$

If we write the free energy explicitly in terms of Σ_k and θ_k, we immediately see that it can be factorized with products of exponential functions, each depending only on a single Σ_k and the respective parameter θ_k. In other words, parameters θ_k are independent and their likelihood is only effected by the respective Σ_k. Indeed, we have that

$$p(\boldsymbol{\theta}|\boldsymbol{\Sigma}) = \frac{e^{-\widehat{F}(\boldsymbol{\Sigma}|\boldsymbol{\theta})}}{Z(\boldsymbol{\Sigma})} = \frac{e^{-\sum_{k=1}^{K}\theta_k\Sigma_k}}{\int_{\Theta} e^{-\sum_{k=1}^{K}\theta_k\Sigma_k}\, \boldsymbol{d\theta}} = \prod_{k=1}^{K} \frac{e^{-\theta_k\Sigma_k}}{\int_{\Theta_k} e^{-\theta_k\Sigma_k}\, d\theta_k}. \tag{3.8}$$

Therefore, we can introduce the probabilities of each parameter θ_k as

$$p_k(\theta_k|\Sigma_k) = \frac{e^{-\theta_k\Sigma_k}}{Z_k(\Sigma_k)}, \tag{3.9}$$

where the normalization factor $Z_k(\Sigma_k)$ can be explicitly computed as

$$Z_k(\Sigma_k) = \int_{\Theta_k} e^{-\theta_k\Sigma_k}\, d\theta_k = -\frac{e^{-\theta_k\Sigma_k}}{\Sigma_k}\Bigg|_{\theta_k^{\min}}^{\theta_k^{\max}} = \frac{e^{-\theta_k^{\min}\Sigma_k} - e^{-\theta_k^{\max}\Sigma_k}}{\Sigma_k}. \tag{3.10}$$

Finally, the independence of parameters θ_k is clear, as

$$p(\boldsymbol{\theta}|\boldsymbol{\Sigma}) = \prod_{k=1}^{K} p_k(\theta_k|\Sigma_k)$$

3.2.3 Parameter estimation and uncertainty quantification

Bayesian inference provide an explicit probability distribution of the parameters $\boldsymbol{\theta}$ in terms of the summary statistics $\boldsymbol{\Sigma}(\boldsymbol{\phi})$, that can be computed from the observed configuration. This provides not only a point estimate for each parameter, but also a measure of uncertainty associated with the estimation.

The expected value of θ_k, conditioned on the observed summary statistic Σ_k, serves a natural estimator and can be computed explicitly, as

$$\begin{aligned}\mathrm{E}\left[\theta_k|\Sigma_k\right] &= \int_{\theta_k^{\min}}^{\theta_k^{\max}} \theta_k p_k(\theta_k|\Sigma_k)\, d\theta_k = \int_{\theta_k^{\min}}^{\theta_k^{\max}} \theta_k \frac{e^{-\theta_k\Sigma_k}}{Z_k(\Sigma_k)}\, d\theta_k \\ &= \frac{1}{Z_k(\Sigma_k)} \int_{\theta_k^{\min}}^{\theta_k^{\max}} \theta_k e^{-\theta_k\Sigma_k}\, d\theta_k = \frac{1}{Z_k(\Sigma_k)} \left[-\frac{e^{-\Sigma_k\theta_k}(\Sigma_k\theta_k+1)}{\Sigma_k^2} \right]_{\theta_k^{\min}}^{\theta_k^{\max}} \\ &= \frac{e^{-\Sigma_k\theta_k^{\min}}(\Sigma_k\theta_k^{\min}+1) - e^{-\Sigma_k\theta_k^{\max}}(\Sigma_k\theta_k^{\max}+1)}{Z_k(\Sigma_k)\Sigma_k^2}\end{aligned}$$

To gain insight into the numerical behavior of the integral, we can rewrite the expected value in a more convenient form, expressing the normalization factor $Z_k(\theta_k)$ through Eq. (3.10)

$$\begin{aligned}E[\theta_k|\Sigma_k] &= \frac{e^{-\theta_k^{\min}\Sigma_k} - e^{-\theta_k^{\max}\Sigma_k} + \Sigma_k(\theta_k^{\min}e^{-\theta_k^{\min}\Sigma_k} - \theta_k^{\max}e^{-\theta_k^{\max}\Sigma_k})}{(e^{-\theta_k^{\min}\Sigma_k} - e^{-\theta_k^{\max}\Sigma_k})\Sigma_k} \\ &= \frac{1}{\Sigma_k} + \frac{\theta_k^{\min}e^{-\theta_k^{\min}\Sigma_k} - \theta_k^{\max}e^{-\theta_k^{\max}\Sigma_k}}{e^{-\theta_k^{\min}\Sigma_k} - e^{-\theta_k^{\max}\Sigma_k}} \\ &= \frac{1}{\Sigma_k} + \frac{\theta_k^{\min} - \theta_k^{\max}e^{-\Sigma_k\Delta\theta_k}}{1 - e^{-\Sigma_k\Delta\theta_k}},\end{aligned} \tag{3.11}$$

where we introduced $\Delta\theta_k := \theta_k^{\max} - \theta_k^{\min}$.

We consider now two limiting cases: $\Sigma_k\Delta\theta_k \ll 0$ and $\Sigma_k\Delta\theta_k \gg 0$. For $\Sigma_k\Delta\theta_k \ll 0$, we have that Σ_k is negative and large in magnitude, meaning that the state summary statistic Σ_k favors larger values of θ_k, as approximating the conditional expected value in this regime, we get

$$\mathrm{E}\left[\theta_k|\Sigma_k\right] \approx \frac{1}{\Sigma_k} + \theta_k^{\max}.$$

Thus, in the case where Σ_k is is strongly negative, the expected value of θ_k is primarily influenced by the upper bound of the prior interval $\theta_k^{\max}$, which can result in an artificial skew toward large parameter values. Conversely, for $\Sigma_k\Delta\theta_k \gg 0$, the summary statistic Σ_k is positive and large, leading to the simplified expectation

$$\mathrm{E}\left[\theta_k|\Sigma_k\right] \approx \frac{1}{\Sigma_k} + \theta_k^{\min}.$$

Here, the inferred value of θ_k are biased toward the lower bound $\theta_k^{\min}$, which can lead to an underestimation of the parameter in cases where the likelihood suggests large values.

These limiting cases illustrate that the choice of prior intervals Θ_k significantly influences parameter inference, especially in cases where the summary statistic Σ_k has a large magnitude.

Finally, the Bayesian framework also allows us to quantify the uncertainty of each estimated parameter by computing its posterior variance. The variance of θ_k, conditioned on Σ_k, is given by

$$\mathrm{Var}(\theta_k|\Sigma_k) = \mathrm{E}\left[\theta_k^2|\Sigma_k\right] - \mathrm{E}\left[\theta_k|\Sigma_k\right]^2,$$

where $\mathrm{E}\left[\theta_k|\Sigma_k\right]$ has been already computed and

$$\begin{aligned}
\mathrm{E}\left[\theta_k^2|\Sigma_k\right] &= \int_{\theta_k^{\min}}^{\theta_k^{\max}} \theta_k^2 p_k(\theta_k|\Sigma_k)\, d\theta_k = \frac{1}{Z_k(\Sigma_k)} \int_{\theta_k^{\min}}^{\theta_k^{\max}} \theta_k^2 e^{-\Sigma_k\theta_k}\, d\theta_k \\
&= \frac{1}{Z_k(\theta_k)} \left[-\frac{e^{-\Sigma_k\theta_k}(\Sigma_k^2\theta_k^2 + 2\Sigma_k\theta_k + 2)}{\Sigma_k^3} \right]_{\theta_k^{\min}}^{\theta_k^{\max}} \\
&= \frac{e^{-\Sigma_k\theta_k^{\min}}\left(\Sigma_k^2(\theta_k^{\min})^2 + 2\Sigma_k\theta_k^{\min} + 2\right) - e^{-\Sigma_k\theta_k^{\max}}\left(\Sigma_k^2(\theta_k^{\max})^2 + 2\Sigma_k\theta_k^{\max} + 2\right)}{Z_k(\Sigma_k)\Sigma_k^3}
\end{aligned}$$

which can also be written expressing the normalization factor $Z_k(\theta_k)$ through Eq. (3.10)

$$\begin{aligned}
\mathrm{E}\left[\theta_k^2|\Sigma_k\right] &= \frac{e^{-\Sigma_k\theta_k^{\min}}\left(\Sigma_k^2(\theta_k^{\min})^2 + 2\Sigma_k\theta_k^{\min} + 2\right) - e^{-\Sigma_k\theta_k^{\max}}\left(\Sigma_k^2(\theta_k^{\max})^2 + 2\Sigma_k\theta_k^{\max} + 2\right)}{(e^{-\theta_k^{\min}\Sigma_k} - e^{-\theta_k^{\max}\Sigma_k})\Sigma_k^2} \\
&= \frac{2}{\Sigma_k} + \frac{2}{\Sigma_k}\frac{\theta_k^{\min} - \theta_k^{\max}e^{-\Sigma_k\Delta\theta_k}}{1 - e^{-\Sigma_k\Delta\theta_k}} + \frac{(\theta_k^{\min})^2 - (\theta_k^{\max})^2 e^{-\Sigma_k\Delta\theta_k}}{1 - e^{-\Sigma_k\Delta\theta_k}}
\end{aligned} \tag{3.12}$$

Therefore, putting together Eq. (3.12) and (3.11), the variance can be expressed as

$$\mathrm{Var}(\theta_k|\Sigma_k) = \frac{1}{\Sigma_k^2} + \frac{(\theta_k^{\min})^2 - (\theta_k^{\max})^2 e^{-\Sigma_k\Delta\theta_k}}{1 - e^{-\Sigma_k\Delta\theta_k}} - \left(\frac{\theta_k^{\min} - \theta_k^{\max}e^{-\Sigma_k\Delta\theta_k}}{1 - e^{-\Sigma_k\Delta\theta_k}} \right)^2 \tag{3.13}$$

Chapter 4

Experiments

Modern techniques of microscopy allow us to obtain high-resolution imaging data of nucleoli structures. In particular, AiryScan confocal microscopy is a super-resolution optical imaging method, that allows to visualize morphological features beyond the diffraction limit of light [24].

Here, we analyze three-dimensional fluorescence microscopy images of HeLa cells, a well-established human cell line widely used in biological research. The images are collected using AiryScan technology on a three-dimensional rectangular domain discretized into $372 \times 372 \times 42$ voxels, with a voxel size of $42.5 \times 42.5 \times 170$ nm. Due to the optical properties of fluorescence microscopy, resolution is higher in the xy plane than along the z-axis, leading to an anisotropic scaling in the reconstructed images. As a result, nucleolar structures often appear elongated along the z-axis when visualized in three dimensions, requiring a proper scaling for accurate representation.

(a) Dense Fibrillar Component (b) Fibrillar Center (c) Granular Component

Figure 4.1: Three-dimensional fluorescence microscopy images of nucleolar components in HeLa cells, acquired using AiryScan confocal microscopy.

The available dataset [11] consists of fluorescence intensity fields for the three primary nucleolar components, as shown in Figure 4.1. However, these images do not contain explicit information on the distribution of the surrounding nucleoplasm. Since our phase separation model is based on volume fraction fields, we must convert fluorescence intensities into estimates of volume fractions for each nucleolar component.

4.1 Conversion of intensities to volume fractions

The three-dimensional microscopy snapshot represents an equilibrium state of a four-component system consisting of the three nucleolar components and the surrounding nucleoplasm. To estimate volume fractions, we start denoting the available intensity fields with $I_a(\boldsymbol{x})$ for each nucleolar components $a \in \mathcal{A}_C = \{1,2,3\}$. The imaging data are discretized over a domain Ω of volume $|\Omega|$ and voxel size ω and the field of intensities is sampled in the centers of each voxel, so that $\boldsymbol{x} \in \{\boldsymbol{x_m}\}_{\boldsymbol{m} \in \boldsymbol{M}}$.

To convert fluorescence intensities into volume fractions, we utilize biophysical properties of nucleolar and nucleoplasmic proteins reported in the literature. Specifically, we extract values for the radius of gyration R_a [16] of the proteins and their average concentrations ζ_a [17].

The proteins that constitute the three main nucleolar substructures, labeled in $\mathcal{A}_C$, have distinct sizes and concentrations in the nucleolus. In Table 4.1 we report their experimental estimates.

Protein	UniprotID	R_g (Å)	ζ (nM)
NPM1 (GC)	P06748	37.57	26740.4
FBL (DFC)	P22087	27.06	2150.7
UBF (FC)	P17480	46.09	600.8

Table 4.1: Radius of gyration and concentration of proteins associated with the three nucleolar components.

In addition to nucleolar components, the nucleoplasm contains a variety of proteins. Table 4.2 summarizes the radius of gyration and concentrations for a choice of the three most abundant nucleoplasmic proteins.

Protein	UniprotID	R_g (Å)	ζ (nM)
HNRNP A2/B1	P22626	37.42	15292.5
HNRNP C1/C2	P07910	42.07	11598.6
HNRNP H1	P31943	37.00	4792.5

Table 4.2: Radius of gyration and concentration of three of the most abundant nucleoplasmic proteins.

The volume of an individual protein molecule of each component can be estimated using the standard formula for the volume of a sphere, so that for $a \in \mathcal{A}_C$ we have

$$v_a = \frac{4}{3}\pi R_a^3.$$

Similarly, the nucleoplasm is characterized by an average protein radius of gyration R_C and an effective concentration ζ_C, that can be computed averaging the values reported in Table4.2. Likewise, we denote the estimate of the volume of proteins in the nucleoplasm as v_C.

Using these parameters, the expected total volume occupied by proteins in the system (both nucleolar and nucleoplasmic) can be estimated as

$$U = N_{\mathrm{A}} \sum_{a \in \mathcal{A}} v_a \zeta_a,$$

where N_{A} denotes the Avogadro constant. From this, the total number of molecules in the domain can be estimated as $N_{\mathrm{A}}\zeta_a|\Omega|/U$. Multiplying by the molecular volume v_a, we get the total volume occupied by each component

$$r_a = N_{\mathrm{A}}\zeta_a \frac{|\Omega|}{U} v_a.$$

Since fluorescence intensities do not directly correspond to volume fractions, we first normalize the intensity fields for each component $a \in \mathcal{A}_C$ as

$$I_a^{\mathrm{norm}}(\boldsymbol{x}) = \frac{I_a(\boldsymbol{x})}{\sum_{\boldsymbol{y} \in \{\boldsymbol{x_m}\}} I_a(\boldsymbol{y})},$$

for $\boldsymbol{x_m} \in \{\boldsymbol{x_m}\}_{\boldsymbol{m} \in \boldsymbol{M}}$.

Using these normalized intensities, we define an initial estimate of the volume fraction field as

$$\widetilde{\phi}_a(\boldsymbol{x}) = I_a^{\mathrm{norm}}(\boldsymbol{x}) \frac{r_a}{\omega}.$$

Since the fluorescence intensity of the nucleoplasm is not explicitly available, we need to apply a rescaling procedure to ensure that the volume fractions sum to unity. Assuming that there exists at least one voxel in the domain where the nucleoplasm volume fraction is zero, we define the final corrected volume fraction field for $a \in \mathcal{A}_C$ as

$$\phi_a(\boldsymbol{x}) = \frac{\widetilde{\phi}_a(\boldsymbol{x})}{\max_{\boldsymbol{y} \in \{\boldsymbol{x_m}\}} \left[\sum_{b \in \mathcal{A}_C} \widetilde{\phi}_b(\boldsymbol{y}) \right]}.$$

Finally, the volume fraction of the nucleoplasm can be computed using the constraint (2.1).

4.2 Estimation results

After converting fluorescence intensities into volume fraction fields, we applied the least squares method to infer the interaction parameters χ_{ab}, which characterize the thermodynamic interactions between the nucleolar components and the surrounding nucleoplasm.

The estimation was performed under two different modeling assumptions: a quaternary mixture, where the system was treated as a four-component mixture consisting of the three nucleolar components and the surrounding nucleoplasm, and a binary approximation, where the nucleolar components were combined into a single phase distinct from the nucleoplasm, reducing the system to a binary mixture.

In both models, values for the molecular size ratios N_a and and gradient coefficients κ_{ab} were not inferred, but defined based on literature knowledge, to reduce the number of free parameters and improve the reliability of the least squares estimation. The molecular size ratios N_a were derived from the radii of gyration R_a reported in Table 4.1 and Table 4.2. Since the Flory-Huggins theory defines N_a as as the volume ratio relative to the solvent phase, they were computed using the relation

$$N_a = \frac{v_a}{v_C} = \frac{R_a^3}{R_C^3},$$

where v_a represents the estimated volume of the protein species $a \in \mathcal{A}_C$ and v_C corresponds to the average volume of the most abundant nucleoplasmic proteins.

For the gradient coefficients κ_{ab}, we assumed a relationship with interaction parameters χ_{ab} and radii of gyration R_a, as described in Eq. (3.4), following a model previously proposed in the literature.

4.2.1 Quaternary model

The first approach considered a four-component system, where each nucleolar substructure was treated as a distinct phase. Using the converted volume fraction fields, predefined values of N_a and the relation of κ_{ab} in terms of χ_{ab}, we applied the least squares method to infer the interaction parameters χ_{ab}.

The inferred values are summarized in Table 4.3, while the values of the predefined parameters κ_{ab} and N_a are reported in Table 4.4

Parameter	Estimate	Standard Error (%)
χ_{12}	55.88	4.05
χ_{13}	214.13	1.27
χ_{14}	4.72	2.15
χ_{23}	188.61	3.11
χ_{24}	53.82	4.19
χ_{34}	214.76	1.25

Table 4.3: Inferred interaction parameters, applying the least squares method to a fluorescence microscopy image of nucleolar component and interpreting the system as a quaternary mixture.

Parameter	Value
κ_{11}	7.66×10^{-6}
κ_{12}	3.25×10^{-6}
κ_{13}	9.95×10^{-6}
κ_{22}	1.09×10^{-4}
κ_{23}	3.83×10^{-5}
κ_{33}	2.67×10^{-4}
N_1	0.90
N_2	1.65
N_3	0.33

Table 4.4: Defined values of the gradient coefficients κ_{ab} and the molecular size ratios N_a used in the quaternary mixture model to infer χ_{ab} applying least squares method. The values of κ_{ab} are computed using an empirical relation in terms of the inferred interaction parameters χ_{ab}, while N_a is estimated from the molecular radii of gyration extracted from literature data.

4.2.2 Binary model

To explore a simplified description of nucleolar organization, we also tested a binary approximation, where the three nucleolar components were treated as a single phase distinct from the nucleoplasm. This reduced the number of inferred parameters to a single interaction parameter χ, simplifying the model significantly.

To construct the binary volume fraction fields, the nucleolar components were combined into a single phase

$$\phi_1^{\text{bin}} = \sum_{a \in \mathcal{A}_C} \phi_a.$$

The volume fraction of the nucleoplasm remains unchanged, defined as $\phi_2^{\text{bin}} = 1 - \phi_1^{\text{bin}}$.

The effective molecular size ratio N_1^{bin} for the nucleolar phase was computed as the average of the sizes of nucleolar components:

$$N_1^{\text{bin}} = \frac{1}{3} \sum_{a \in \mathcal{A}_C} N_a.$$

Similarly, the gradient coefficient κ was determined using the relation (3.4).

Using the volume fraction fields ϕ_a^{bin} for $a \in \{1,2\}$, the relative size N_1^{bin} and the form of the gradient coefficient κ, we used the least squares method to estimate the interaction parameter χ. The inferred interaction parameter χ for the binary model is reported in Table 4.5, while the predefined values of the relative size N_1^{bin} and the gradient coefficient κ are reported in Table 4.6.

Parameter	Estimate	Standard Error (%)
χ	3.79	0.72

Table 4.5: Inferred interaction parameters, applying the least squares method to a fluorescence microscopy image of nucleolar component and interpreting the system as a binary mixture.

Parameter	Value
κ	6.05×10^{-6}
N_1^{bin}	0.96

Table 4.6: Defined values of the gradient coefficients κ and the molecular size ratios N_1 used in the binary mixture model to infer χ applying least squares method. The value of κ is computed using an empirical relation in terms of the inferred interaction parameters χ, while N_1 is estimated from the molecular radii of gyration extracted from literature data.

4.3 Interpretation and limitations

Our findings suggest that an equilibrium Cahn-Hilliard model based solely on the inferred interaction parameters does not fully capture the complexity of nucleolar phase separation.

To assess whether the inferred parameters could reproduce experimental observations, we performed numerical simulations of the quaternary and binary mixtures using the Cahn-Hilliard model. The system was evolved both from the volume fraction fields computed from microscopy data—assuming they represent an equilibrium state—and from a uniform initial condition with small random noise.

When initialized from a homogeneous state with added noise, the system does not evolve into large, well-defined compartments. Instead, the components segregate at the voxel scale, forming a pattern where each voxel is dominated by a single component without significant aggregation of the nucleolar phase. This outcome suggests that the inferred interaction parameters, while consistent with the least squares estimation framework, do not lead to spontaneous phase separation under the Cahn-Hilliard dynamics. Figure 4.2 illustrates the final state binary mixture model when evolved from a uniform initial condition with Gaussian noise. The lack of clear domain formation in these simulations indicates that thermodynamic interactions alone may not be sufficient to drive nucleolar phase separation.

When the simulations are instead initialized from the volume fraction fields inferred from microscopy images, the system evolves differently. Components tend to contract into smaller, more localized regions, sharpening the boundaries between different phases. The evolution leads to configurations that are more strongly segregated than in the experimental data, where interfaces are more diffuse and components remain partially mixed. This effect is particularly evident in Figure 4.3, where the nucleolar compartments become

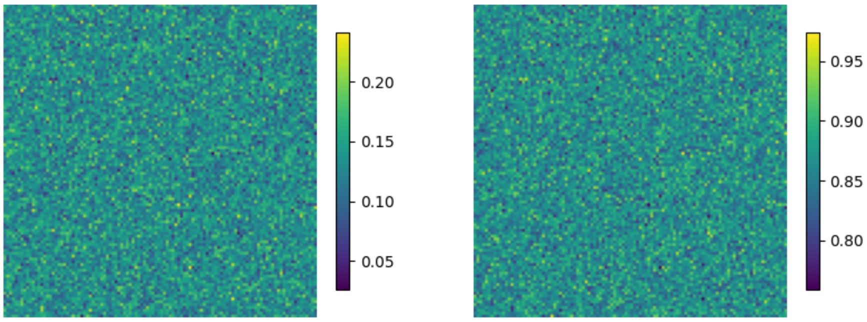

(a) Initial state at time $t = 0$.

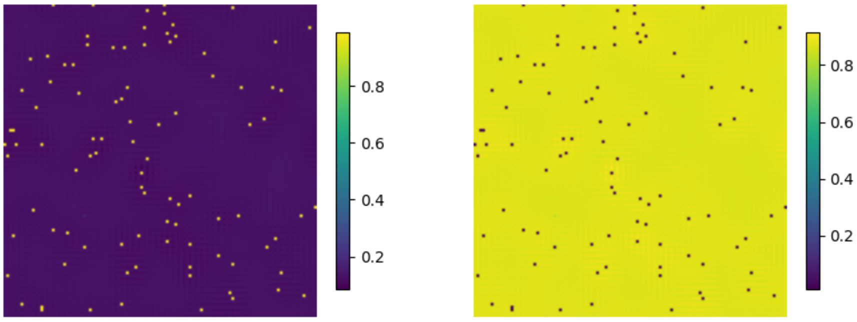

(b) Final state at time $t = 10000000$

Figure 4.2: Evolution of volume fractions in a binary mixture within a three-dimensional domain, according to Cahn-Hilliard model. Simulation start from an initial uniform state with Gaussian noise and parameters are inferred from experimental data, using least square method. In the images are reported the maximum intensity slices of initial and final state.

more confined compared to the initial state.

This behavior suggests that either the inferred interaction parameters overestimate the

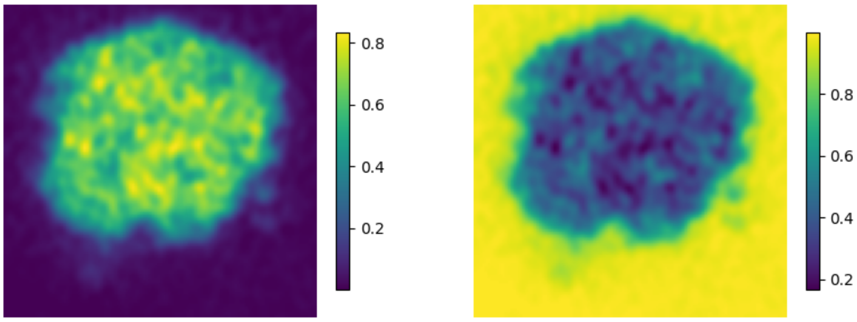

(a) Initial state at time $t = 0$.

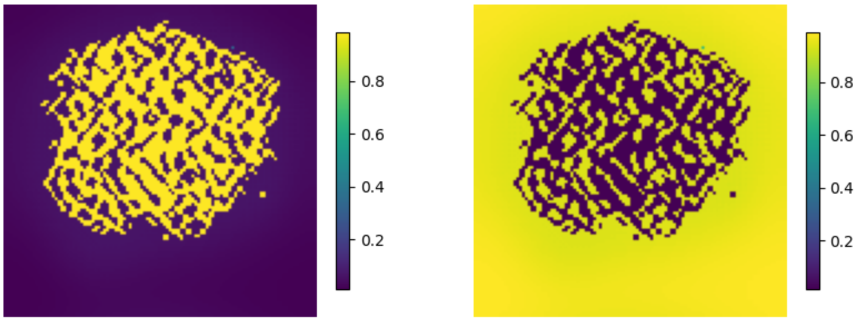

(b) Final state at time $t = 10000000$

Figure 4.3: Evolution of volume fractions in a binary mixture within a three-dimensional domain, according to Cahn-Hilliard model. Simulation start from the state defined by experimental data and parameters are inferred using least square method from the same state. In the images are reported the maximum intensity slices of initial and final state.

strength of phase separation or that the experimental volume fraction fields do not truly represent an equilibrium state, but rather a transient or locally stabilized configuration.

A key observation from the gradient coefficients is that the values of κ_{ab} are around five order of magnitude smaller than other parameters χ_{ab} and N_a. Such small κ values indicate that the cost of creating interfaces is low, meaning that many small regions of different phases can coexist with minimal energetic penalty. This translates to a system with weak surface tension, leading to suppressed domain coarsening and an overall lack of Ostwald ripening. As a result, even if the system initially forms small nucleolar-like structures, they do not grow or coalesce over time into well defined domains, as one would expect in classical phase separation.

Another critical observation from the computed volume fractions is that, when considering only the three nucleolar component, they do not seem to separate from one another. Instead they appear to mix, with the GC being predominant throughout the nucleolus and the other components—FC and DFC— present only in smaller amounts. This suggest that the phase separation between nucleolar component is either weak or absent. The lack of distinct subdomains within the nucleolus challenges the assumption that phase separation alone is sufficient to explain its internal organization. This observation also motivated the alternative approach of modeling nucleolar organization as a binary phase separation between nucleolus and nucleoplasm, rather than as a fully quaternary system. By treating the nucleolus as a single effective phase rather than a mixture of three coexisting components, the binary model aims to capture the dominant separation between nucleolar and nucleoplasmic regions.

These results indicate two main possibilities. First, the simulated evolution from a uniform initial condition may lead to a local equilibrium that is different from the experimentally observed configuration, meaning that the system could be trapped in a metastable state rather than reaching a global thermodynamic equilibrium. Alternatively, the fluorescence data themselves might not represent an equilibrium state but rather a steady state configuration maintained by active cellular processes. This interpretation aligns with biological evidence suggesting that nucleolar structures are stabilized by ATP-dependent processes such as RNA transcription, processing, and ribosome assembly.

Overall, our findings demonstrate that while the inferred parameters provide a mathematically consistent equilibrium description, the resulting Cahn–Hilliard simulations do not fully reproduce the experimentally observed nucleolar morphology. This discrepancy suggests that nucleolar organization may be governed by active processes beyond simple phase separation.

Conclusion and future research

In this work, we developed a theoretical and computational framework to model liquid-liquid phase separation in multicomponent systems, applying it to the organization of nucleolar compartments. We combined Flory-Huggins thermodynamics and Cahn-Hilliard dynamics to describe phase separation phenomena and employed both deterministic numerical methods and stochastic sampling techniques to investigate equilibrium configurations. Our approach integrated theoretical modeling with data-driven parameter inference, bridging the gap between experimental data and physical mechanisms governing liquid-liquid phase separation.

Incorporating stochastic fluctuations through the Metropolis-Hastings algorithm allowed us to explore equilibrium sampling and assess the role of thermal noise in the system. However, full convergence of the Metropolis-Hastings method proved computationally demanding when starting from a homogeneous state, hinting the need to use a Cahn-Hilliard pre-equilibrated state as a reference.

To validate our parameter estimation techniques, we first applied them to synthetic equilibrium states generated with known parameters. The methods proved effective in recovering these values, confirming their robustness. We then applied the same approach to experimental microscopy data, converting fluorescence intensities into volume fractions and inferring the interaction parameters. A key challenge in this process was the absence of explicit nucleoplasmic intensity measurements, which required rescaling procedures and careful interpretation of volume fraction distributions.

Our results suggest that the equilibrium model of a four-component protein solution is not sufficient to fully explain the observed nucleolar structures. Using the developed estimation techniques, we inferred the interaction parameters governing equilibrium configurations. These values suggest that molecular interactions alone may not account for the stability and organization of nucleolar subcompartments. Our findings indicate that additional mechanisms, such as RNA transcription, processing, and ribosome assembly, likely contribute to maintaining the spatial organization of the nucleolus beyond what is predicted by equilibrium thermodynamics. The small values of the gradient coefficients κ obtained from our inference suggest that the nucleolar components exhibit a weak tendency for droplet coarsening, limiting Ostwald ripening and stabilizing small-scale structures. This observation further supports the hypothesis that active biological processes play a crucial role in nucleolar organization.

While our study has provided insights into the equilibrium properties of nucleolar phase separation, several important questions remain open. Future research could extend this framework to incorporate active processes, such as ATP-dependent reactions and RNA fluxes, which are essential for understanding the full dynamics of nucleolar formation. Additionally, incorporating more detailed molecular interactions may refine our model's accuracy. Experimental validation through perturbation studies, where key molecular components are selectively inhibited or enhanced, could further test the predictive power of our approach.

In conclusion, this work has contributed to the understanding of biomolecular phase separation by integrating thermodynamic modeling, computational simulations, and data-driven inference methods. While equilibrium models alone may not fully capture the complexity of nucleolar structure, they provide a solid foundation for future research incorporating active biological processes. Beyond nucleolar organization, we have laid the groundwork for further studies, building a framework that is broadly applicable to various phase separation phenomena in both biological and non-biological contexts. The insights gained from this study have implications not only for cellular organization but also for fields such as materials science and biomedical engineering, where phase separation plays a crucial role in designing functional materials and understanding self-assembling systems.

Bibliography

[1] Kamal Asadi, Dago M. de Leeuw, Bert de Boer, and Paul W. M. Blom. Organic non-volatile memories from ferroelectric phase-separated blends. *Nature Materials*, 7(7):547–550, June 2008. ISSN 1476-4660. doi: 10.1038/nmat2207. URL http://dx.doi.org/10.1038/nmat2207.

[2] Clifford P. Brangwynne, Timothy J. Mitchison, and Anthony A. Hyman. Active liquid-like behavior of nucleoli determines their size and shape in xenopus laevis oocytes. *Proceedings of the National Academy of Sciences*, 108(11):4334–4339, February 2011. ISSN 1091-6490. doi: 10.1073/pnas.1017150108. URL http://dx.doi.org/10.1073/pnas.1017150108.

[3] John W. Cahn and John E. Hilliard. Free energy of a nonuniform system. i. interfacial free energy. *The Journal of Chemical Physics*, 28(2):258–267, February 1958. ISSN 1089-7690. doi: 10.1063/1.1744102. URL http://dx.doi.org/10.1063/1.1744102.

[4] J. Clerk-Maxwell. On the dynamical evidence of the molecular constitution of bodies *. *Nature*, 11(279):357–359, March 1875. ISSN 1476-4687. doi: 10.1038/011357a0. URL http://dx.doi.org/10.1038/011357a0.

[5] H.E Cook. Brownian motion in spinodal decomposition. *Acta Metallurgica*, 18(3): 297–306, March 1970. ISSN 0001-6160. doi: 10.1016/0001-6160(70)90144-6. URL http://dx.doi.org/10.1016/0001-6160(70)90144-6.

[6] P. Debye. Angular dissymmetry of the critical opalescence in liquid mixtures. *The Journal of Chemical Physics*, 31(3):680–687, September 1959. ISSN 1089-7690. doi: 10.1063/1.1730446. URL http://dx.doi.org/10.1063/1.1730446.

[7] Carsten Deibel and Vladimir Dyakonov. Polymer–fullerene bulk heterojunction solar cells. *Reports on Progress in Physics*, 73(9):096401, August 2010. ISSN 1361-6633. doi: 10.1088/0034-4885/73/9/096401. URL http://dx.doi.org/10.1088/0034-4885/73/9/096401.

[8] Paul J. Flory. Thermodynamics of high polymer solutions. *The Journal of Chemical Physics*, 10(1):51–61, January 1942. ISSN 1089-7690. doi: 10.1063/1.1723621. URL http://dx.doi.org/10.1063/1.1723621.

[9] Majid Hassanizadeh and William G Gray. General conservation equations for multiphase systems: 1. averaging procedure. *Advances in Water Resources*, 2:131–144, March 1979. ISSN 0309-1708. doi: 10.1016/0309-1708(79)90025-3. URL `http://dx.doi.org/10.1016/0309-1708(79)90025-3`.

[10] W. K. Hastings. Monte carlo sampling methods using markov chains and their applications. *Biometrika*, 57(1):97–109, April 1970. ISSN 0006-3444. doi: 10.1093/biomet/57.1.97. URL `http://dx.doi.org/10.1093/biomet/57.1.97`.

[11] Y. Hayashi, C. Bevilacqua, M. Brzezinski, S. H. Parekh, J. Michels, R. Prevedel, and S. Cuylen-Häring. Nucleolus ejects internal components by altering its material properties upon arresting rna flux. In *EMBL symposium: Cellular mechanisms driven by phase separation*, May 2024.

[12] Carsten Hoege and Anthony A. Hyman. Principles of par polarity in caenorhabditis elegans embryos. *Nature Reviews Molecular Cell Biology*, 14(5):315–322, April 2013. ISSN 1471-0080. doi: 10.1038/nrm3558. URL `http://dx.doi.org/10.1038/nrm3558`.

[13] Yutaro Hori, Christoph Engel, and Takehiko Kobayashi. Regulation of ribosomal rna gene copy number, transcription and nucleolus organization in eukaryotes. *Nature Reviews Molecular Cell Biology*, 24(6):414–429, February 2023. ISSN 1471-0080. doi: 10.1038/s41580-022-00573-9. URL `http://dx.doi.org/10.1038/s41580-022-00573-9`.

[14] Maurice L. Huggins. Some properties of solutions of long-chain compounds. *The Journal of Physical Chemistry*, 46(1):151–158, January 1942. ISSN 1541-5740. doi: 10.1021/j150415a018. URL `http://dx.doi.org/10.1021/j150415a018`.

[15] Anthony A. Hyman, Christoph A. Weber, and Frank Jülicher. Liquid-liquid phase separation in biology. *Annual Review of Cell and Developmental Biology*, 30(1):39–58, October 2014. ISSN 1530-8995. doi: 10.1146/annurev-cellbio-100913-013325. URL `http://dx.doi.org/10.1146/annurev-cellbio-100913-013325`.

[16] Neurosnap Inc. Neurosnap tools documentation. `https://github.com/NeurosnapInc/neurosnap`, 2025.

[17] Daniel N Itzhak, Stefka Tyanova, Jürgen Cox, and Georg HH Borner. Global, quantitative and dynamic mapping of protein subcellular localization. *eLife*, 5, June 2016. ISSN 2050-084X. doi: 10.7554/elife.16950. URL `http://dx.doi.org/10.7554/eLife.16950`.

[18] Hideto Matsuyama, Stephane Berghmans, and Douglas R Lloyd. Formation of anisotropic membranes via thermally induced phase separation. *Polymer*, 40(9):2289–2301, April 1999. ISSN 0032-3861. doi: 10.1016/s0032-3861(98)00040-8. URL `http://dx.doi.org/10.1016/S0032-3861(98)00040-8`.

[19] Hideto Matsuyama, Masuo Yuasa, Yoshiro Kitamura, Masaaki Teramoto, and Douglas R Lloyd. Structure control of anisotropic and asymmetric polypropylene membrane prepared by thermally induced phase separation. *Journal of Membrane Science*, 179(1–2):91–100, November 2000. ISSN 0376-7388. doi: 10.1016/s0376-7388(00)00506-8. URL `http://dx.doi.org/10.1016/S0376-7388(00)00506-8`.

[20] E.Bruce Nauman and David Qiwei He. Morphology predictions for ternary polymer blends undergoing spinodal decomposition. *Polymer*, 35(11):2243–2255, May 1994. ISSN 0032-3861. doi: 10.1016/0032-3861(94)90757-9. URL `http://dx.doi.org/10.1016/0032-3861(94)90757-9`.

[21] E.Bruce Nauman and David Qiwei He. Nonlinear diffusion and phase separation. *Chemical Engineering Science*, 56(6):1999–2018, March 2001. ISSN 0009-2509. doi: 10.1016/s0009-2509(01)00005-7. URL `http://dx.doi.org/10.1016/S0009-2509(01)00005-7`.

[22] Mark OJ Olson and Miroslav Dundr. *Nucleolus: Structure and Function*, page 1–9. Wiley, February 2015. ISBN 9780470015902. doi: 10.1002/9780470015902.a0005975.pub3. URL `http://dx.doi.org/10.1002/9780470015902.a0005975.pub3`.

[23] W. Ostwald. Studien über die bildung und umwandlung fester körper: 1. abhandlung: Übersättigung und Überkaltung. *Zeitschrift für Physikalische Chemie*, 22U(1):289–330, February 1897. ISSN 0942-9352. doi: 10.1515/zpch-1897-2233. URL `http://dx.doi.org/10.1515/zpch-1897-2233`.

[24] Ingrid C. Romero, Michael A. Urban, and Surangi W. Punyasena. Airyscan superresolution microscopy: A high-throughput alternative to electron microscopy for the visualization and analysis of fossil pollen. *Review of Palaeobotany and Palynology*, 276:104192, May 2020. ISSN 0034-6667. doi: 10.1016/j.revpalbo.2020.104192. URL `http://dx.doi.org/10.1016/j.revpalbo.2020.104192`.

[25] A. Peter Russo and E. Bruce Nauman. Modeling the effect of compatibilizers in the coarsening of ternary polymer blends with core-shell morphology. *Journal of Polymer Science Part B: Polymer Physics*, 38(10):1301–1306, May 2000. ISSN 1099-0488. doi: 10.1002/(sici)1099-0488(20000515)38:10<1301::aid-polb50>3.0.co;2-m. URL `http://dx.doi.org/10.1002/(SICI)1099-0488(20000515)38:10<1301::AID-POLB50>3.0.CO;2-M`.

[26] C. Schaefer, J. J. Michels, and P. van der Schoot. Structuring of thin-film polymer mixtures upon solvent evaporation. *Macromolecules*, 49(18):6858–6870, September 2016. ISSN 1520-5835. doi: 10.1021/acs.macromol.6b00537. URL `http://dx.doi.org/10.1021/acs.macromol.6b00537`.

[27] Susan Strome and William B. Wood. Generation of asymmetry and segregation of germ-line granules in early c. elegans embryos. *Cell*, 35(1):15–25, November 1983. ISSN 0092-8674. doi: 10.1016/0092-8674(83)90203-9. URL `http://dx.doi.org/10.1016/0092-8674(83)90203-9`.

[28] Lloyd N. Trefethen. *Spectral Methods in MATLAB*. Society for Industrial and Applied Mathematics, January 2000. ISBN 9780898719598. doi: 10.1137/1.9780898719598. URL `http://dx.doi.org/10.1137/1.9780898719598`.

[29] Dustin Updike and Susan Strome. P granule assembly and function in caenorhabditis elegans germ cells. *Journal of Andrology*, 31(1):53–60, January 2010. ISSN 1939-4640. doi: 10.2164/jandrol.109.008292. URL `http://dx.doi.org/10.2164/jandrol.109.008292`.

[30] E. Voronina, G. Seydoux, P. Sassone-Corsi, and I. Nagamori. Rna granules in germ cells. *Cold Spring Harbor Perspectives in Biology*, 3(12):a002774–a002774, July 2011. ISSN 1943-0264. doi: 10.1101/cshperspect.a002774. URL `http://dx.doi.org/10.1101/cshperspect.a002774`.

[31] Christoph A Weber, David Zwicker, Frank Jülicher, and Chiu Fan Lee. Physics of active emulsions. *Reports on Progress in Physics*, 82(6):064601, April 2019. ISSN 1361-6633. doi: 10.1088/1361-6633/ab052b. URL `http://dx.doi.org/10.1088/1361-6633/ab052b`.

[32] Nurit Wolf, James Priess, and David Hirsh. Segregation of germline granules in early embryos ofcaenorhabditis elegans: an electron microscopic analysis. *Development*, 73(1):297–306, February 1983. ISSN 1477-9129. doi: 10.1242/dev.73.1.297. URL `http://dx.doi.org/10.1242/dev.73.1.297`.

[33] Noah Ziethen, Jan Kirschbaum, and David Zwicker. Nucleation of chemically active droplets. *Physical Review Letters*, 130(24), June 2023. ISSN 1079-7114. doi: 10.1103/physrevlett.130.248201. URL `http://dx.doi.org/10.1103/PhysRevLett.130.248201`.

[34] David Zwicker. py-pde: A python package for solving partial differential equations. *Journal of Open Source Software*, 5(48):2158, 2020. doi: 10.21105/joss.02158. URL `https://doi.org/10.21105/joss.02158`.